OPEN ACCESS

Critical elements in non-sulfide Zn deposits: a reanalysis of the Kabwe Zn-Pb ores (central Zambia)

N. Mondillo[1,*], R. Herrington[2], A. J. Boyce[3], C. Wilkinson[2], L. Santoro[2] and M. Rumsey[2]

[1] Dipartimento di Scienze della Terra, dell'Ambiente e delle Risorse, Università degli Studi di Napoli Federico II, Complesso Universitario di Monte Sant'Angelo, Via Cintia, Napoli 80126, Italy
[2] Department of Earth Sciences, Natural History Museum, Cromwell Road, London SW7 5BD, UK
[3] Scottish Universities Environmental Research Centre, East Kilbride G75 0QF, UK

ABSTRACT

The Kabwe Zn-Pb deposit (central Zambia) consists of a cluster of mixed sulfide and non-sulfide orebodies. The sulfide ores comprise sphalerite, galena, pyrite, chalcopyrite and accessory Ge-sulfides (±Ga and In). The non-sulfide ores comprise: (1) willemite-dominated zones encasing massive sulfide orebodies and (2) oxide-dominated alteration bands, overlying both the sulfide and Zn-silicate orebodies. This study focuses on the Ge, In and Ga distribution in the non-sulfide mineralization, and was carried out on a suite of Kabwe specimens, housed in the Natural History Museum Ore Collection (London). Petrography confirmed that the original sulfides were overprinted by at least two contrasting oxidation stages dominated by the formation of willemite (W1 and W2), and a further event characterized by weathering-related processes. Oxygen isotopic analyses have shown that W1 and W2 are unrelated genetically and furthermore not related to supergene Zn-Pb-carbonates in the oxide-dominated assemblage. The $\delta^{18}O$ composition of 13.9–15.7‰ V-SMOW strongly supports a hydrothermal origin for W1. The $\delta^{18}O$ composition of W2 (−3.0‰ to 0‰ V-SMOW) indicates that it precipitated from groundwaters of meteoric origin in either a supergene or a low-T hydrothermal environment. Gallium and Ge show a diversity of distribution among the range of Zn-bearing minerals. Gallium has been detected at the ppm level in W1, sphalerite, goethite and hematite. Germanium occurs at ppm levels in W1 and W2, and in scarcely detectable amounts in hemimorphite, goethite and hematite. Indium has low concentrations in goethite and hematite. These different deportments among the various phases are probably due to the different initial Ga, In and Ge abundances in the mineralization, to the different solubilities of the three elements at different temperatures and pH values, and finally to their variable affinities with the various minerals formed.

KEYWORDS: critical elements, gallium, germanium, Zn deposits, non-sulfides, Kabwe, laser ablation inductively coupled plasma mass spectrometry (LA-ICP-MS), Zambia.

Introduction

THE term 'non-sulfide' is used to define a type of Zn-Pb ore deposit dominated by 'oxidized' Zn and Pb ore minerals, and is applied to distinguish such deposits from entirely sulfide deposits (Large, 2001; Hitzman *et al.*, 2003). Non-sulfide Zn-Pb deposits

*E-mail: nicola.mondillo@unina.it

can be classified into two types: supergene deposits and hypogene deposits, according to their genetic attributes and resultant mineralogies (Large, 2001; Hitzman *et al.*, 2003; Boni and Mondillo, 2015). Supergene deposits form after the weathering and oxidation of exhumed sulfide orebodies at, or close to, the surface, consisting commonly of Zn and Pb carbonates (smithsonite, hydrozincite and cerussite) plus a range of hydrous Zn-bearing silicates and clays (hemimorphite and sauconite), in addition to remnants of primary sulfides (sphalerite, galena and pyrite). Hypogene deposits form either by hydrothermal processes or the metamorphism of primary sulfide ores, and consist mainly of an assemblage of anhydrous Zn silicates and oxides, such as willemite, zincite, franklinite, coexisting locally with sulfides (Hitzman *et al.*, 2003).

The Kabwe Zn-Pb deposit (formerly known as 'Broken Hill') is located in central Zambia, ~110 km north of Lusaka, in an area where several other Fe, Mn, Au and Pb-Zn-Cu-V occurrences are developed (Kampunzu *et al.*, 2009). The mineralized district forms a cluster of mixed sulfide/non-sulfide orebodies. Mineralization was discovered in 1902, and the sulfides were mined until mine closure in 1994 (Kamona and Friedrich, 2007). During its lifespan, Kabwe was the most significant Zn-Pb mine in Zambia, with production from the sulfide bodies of 1.8 Mt of Zn, 0.8 Mt Pb, 79 t Ag, 7820 t V_2O_5, 235 t Cd and 64 t Cu. The sulfide ores included sphalerite, galena, pyrite and chalcopyrite as well as accessory Ge-sulfides (briartite and renierite). Significant Ga and In were also recognized in the ores (Kampunzu *et al.*, 2009). Despite this, these 'critical elements' were never recovered from the mineralization as they were only recognized in 1991, by which time the bulk of the Zn-Pb sulfide orebody was almost completely mined out (Kampunzu *et al.*, 2009). About 1.9 Mt of Zn non-sulfide resources remain with a reported grade of 13.4 wt.% Zn and 1.5 wt.% Pb (Kamona and Friedrich, 2007). This non-sulfide resource consists of (1) Zn-silicate zones mostly containing willemite, which surround the massive Zn-Pb sulfide orebodies, and (2) distinct oxide-rich alteration bands, containing Zn-, Pb- and Cu- vanadates, phosphates and carbonates, overlying both sulfide and Zn-silicate orebodies (Kamona and Friedrich, 2007). In the oxidized zones, willemite and supergene minerals demonstrably formed at the expense of original sulfides (Kamona and Friedrich, 2007; Terracciano, 2008). Although willemite is commonly considered a hydrothermal

mineral (Hitzman *et al.*, 2003, and references therein), a number of authors (Kamona and Friedrich, 2007; Terracciano, 2008) suggest that the willemite at Kabwe may be related to either low-temperature hydrothermal oxidizing fluids or alternatively to weathering processes, particularly given that the willemite at Kabwe is associated with a 'typical' supergene mineral assemblage (e.g. smithsonite, cerussite, goethite).

The aim of the present study was to evaluate Ge, Ga and In related to the non-sulfide mineralization, both in willemite-dominated ore and the oxide-dominated mineral assemblage. For the present study, a reanalysis of Kabwe samples housed in the ore collection of the Natural History Museum, London (NHM) was conducted, with a specific focus on comparing the deportment of trace elements in the primary sulfides and in the oxidized mineral assemblage. In order to better constrain formation processes, oxygen isotope analyses of willemite and other secondary minerals were carried out.

Geological setting

Regional geology

The rocks underlying the Kabwe region are dominated by Neoproterozoic metasediments which unconformably cover a Paleo- to Mesoproterozoic basement consisting of granite gneiss with minor amphibolite, schist, quartzite and pegmatite (Arthurs *et al.*, 1995; Cairney and Kerr, 1998; Kamona and Friedrich, 2007; Kampunzu *et al.*, 2009) (Fig. 1*a*). Neoproterozoic metasedimentary cover rocks are generally considered to be contemporaneous with Katangan rocks of the Copperbelt, formed between 877 and 573 Ma (Cahen *et al.*, 1984; Cairney and Kerr, 1998; Armstrong *et al.*, 1999; Master *et al.*, 2005). According to various authors (Taylor, 1954; Whyte, 1966; Kortman, 1972; Kamona, 1993; Kamona and Friedrich, 2007; Kampunzu *et al.*, 2009), the Neoproterozoic succession in the Kabwe area includes, from the base to the top: (1) a basal conglomerate lying unconformably on the Paleo- to Mesoproterozoic basement complex; (2) a mixed unit known as the Kangomba Formation (Moore, 1964; Cairney and Kerr, 1998) consisting of arkoses, quartzites, conglomerates, metasiltstone, schist, phyllite and dolomite; and (3) a predominantly phyllite-dolomite unit with associated calcite-marble named the Nyama Formation (Moore, 1964; Barr *et al.*, 1978; Intiomale, 1982; Kampunzu *et al.*, 2009). In the Kabwe area (Fig. 1*a*), the upper part
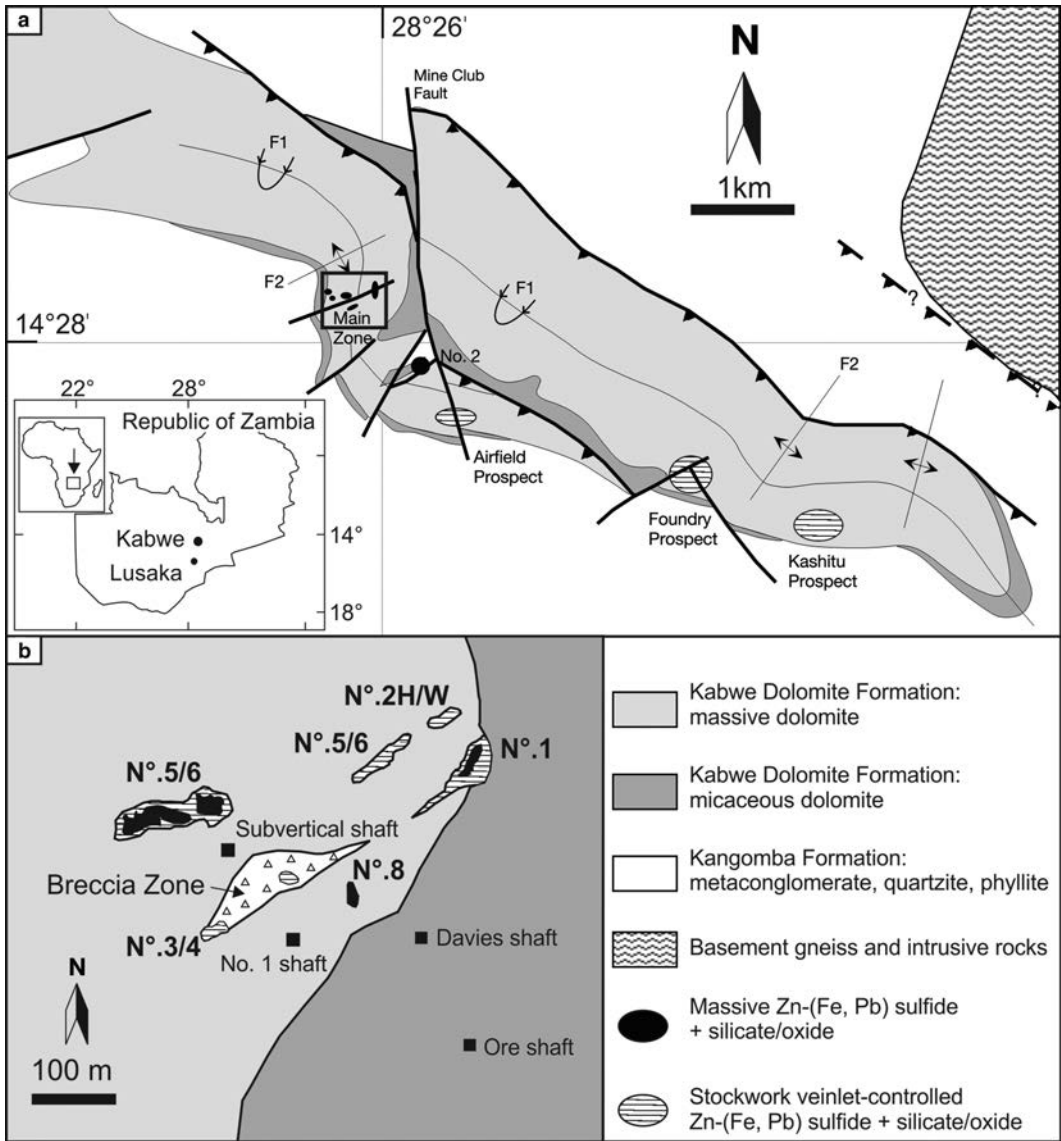
FIG. 1. (*a*) Geological sketch map of the Kabwe area (modified after Hitzman *et al.*, 2003; Kamona and Friedrich, 2007). (*b*) Morphology and relative positions of orebodies on the 850 ft mine level (∼260 m depth from the surface), underlying the surficial Main Zone (black square in (*a*); modified after Kampunzu *et al.*, 2009).

of the Kangomba Formation has been upgraded stratigraphically to a true Formation, named the Kabwe Dolomite Formation, which has been subdivided into two members (Kortman, 1972; Kamona and Friedrich, 2007): (1) the lower micaceous dolomite; and (2) the upper massive dolomite, which hosts the main orebodies (Kamona and Friedrich, 2007).

Main characteristics of the Kabwe mineralization

The morphology, structural setting, mineralogy and geochemistry of the Kabwe orebodies have been described previously by Kamona (1993), Kamona and Friedrich (2007, and references therein), Terracciano (2008) and Kampunzu *et al.* (2009),

and a summary of that work is presented here. The Kabwe primary mineralization is composed of a number of pipe-like bodies of massive Zn-Pb sulfide, containing sphalerite, galena, pyrite, minor chalcopyrite, accessory briartite and the Ge-Cu sulfide renierite, developed in massive dolomite close to the faulted contact with the micaceous dolomite (Kamona, 1993; Kamona and Friedrich, 2007; Kampunzu *et al.*, 2009). These sulfide cores are surrounded locally by strongly oxidized zones mostly consisting of willemite and mineralized jasperoid, with a mixture of quartz, willemite, cerussite, smithsonite, vanadates, phosphates, goethite and hematite.

In detail, (Fig. 1*b*) it is possible to recognize three main massive sulfide orebodies in the Kabwe region referred to as No. 1, No. 3/4 and No. 5/6, all of which occur in highly faulted massive dolomite adjacent to the Mine Club fault zone. The No. 2 body is a willemite-rich but Pb-poor massive orebody. Minor orebodies ("X", "E", South Orebody, No. 2 Hangingwall, No. 8) occur near the main massive sulfide orebodies. Other mineralized occurrences include the small willemite-rich Foundry and the Airfield prospects. Mineralization of the same type is also found a few kilometres from Kabwe (e.g. at Carmarnor, Chowa, Millberg; Kampunzu *et al.*, 2009). The large No. 5/6 and the No. 3/4 orebodies both have pipe-like forms, occur mainly along NE–SW trending faults, and are clearly discordant to the host dolomite (Kamona and Friedrich, 2007). The dolomitic host rock is barren a few metres from the orebodies, rarely containing finely disseminated sphalerite, galena and pyrite. Mineralization at Kabwe is also associated with breccias, which clearly cross-cut the surrounding stratified rocks (Whyte, 1966; Kortman, 1972; Samama *et al.*, 1991; Kamona and Friedrich, 2007).

Primary sulfides (pyrite, sphalerite, galena, chalcopyrite) are recrystallized and deformed (Kamona, 1993; Kamona and Friedrich, 2007). This deformation suggests that the mineralization was affected by a phase of low-grade metamorphism, probably related to the Lufilian orogeny at ~550 Ma., thereby fixing a minimum age for the formation of the sulfide deposit (Porada and Berhorst, 2000; Kamona and Friedrich, 2007). On the basis of Pb isotopic compositions of galena, Kamona *et al.* (1999) proposed a model age for the sulfide mineralization of 680 ± 13 Ma. Summarizing previous works, Kampunzu *et al.* (2009) suggested that the Kabwe mineralization formed from basinal brines during a syntectonic

hydrothermal circulation, which produced carbonate-hosted stratabound epigenetic ore bodies of MVT-type (Leach *et al.*, 2005). On the other hand, some authors (see e.g. Heijlen *et al.*, 2008) consider Kabwe, together with Kipushi, Dikulushi, Lombe, and Kengere, to be a vein-type Zn-Pb-Cu-Ag deposit.

Early, hypogene sulfide minerals are clearly replaced by various secondary minerals (Kamona and Friedrich, 2007; Terracciano, 2008; Kampunzu *et al.*, 2009). In detail, previous work (Kamona and Friedrich 2007, and references therein, Terracciano, 2008) recognized at least two willemite generations: (1) a massive willemite, replacing the sulfides directly, and (2) a crystalline willemite, precipitating in geodes. They also described a range of secondary phases including carbonates (smithsonite, cerussite, azurite, hydrozincite, aurichalcite, rosasite, and Pb- and Zn-malachite), silicates (hemimorphite, chrysocolla), oxides (magnetite, hematite, goethite, zincite, psilomelane, wulfenite and cuprite), rare phosphates (tarbuttite, parahopeite, pyromorphite, hopeite, spencerite, scholzite and zincian libethenite), vanadates (vanadinite, descloizite and mottramite), sulfates (anglesite, gypsum, linarite and goslarite), supergene sulfides (covellite, chalcocite and galena), arsenates (beudantite, mimetite) and native copper. Many of these secondary minerals are typical of a supergene environment and, in fact, occur in a weathering-related alteration profile over sulfides, persisting locally from the surface down to the deepest level of the mine (465 m) (Kamona and Friedrich, 2007; Terracciano, 2008; Kampunzu *et al.*, 2009). Several secondary minerals clearly formed from the mobilization of major and trace elements derived from primary minerals, i.e. arsenates, oxides, carbonates, silicates and sulfides. A limited temporal constraint to the formation of the majority of the supergene minerals at Kabwe is given by ages obtained using U/Th-He methods on descloizite yielding ages of 20–37 Ma (N.J. Evans, unpubl., in Boni *et al.*, 2007).

The processes leading to the formation of willemite are less clear. Willemite could have formed either during *in situ* weathering of the primary sulfide ore and therefore be supergene, or may have formed during hydrothermal alteration of sphalerite, and would thus be hypogene (Kamona and Friedrich, 2007; Terracciano, 2008). Silica occurs partially as quartz and chalcedony in vugs, clearly of supergene origin and introduced into the oxidation zone by circulating groundwaters (Taylor, 1958). However, part of the silica responsible for
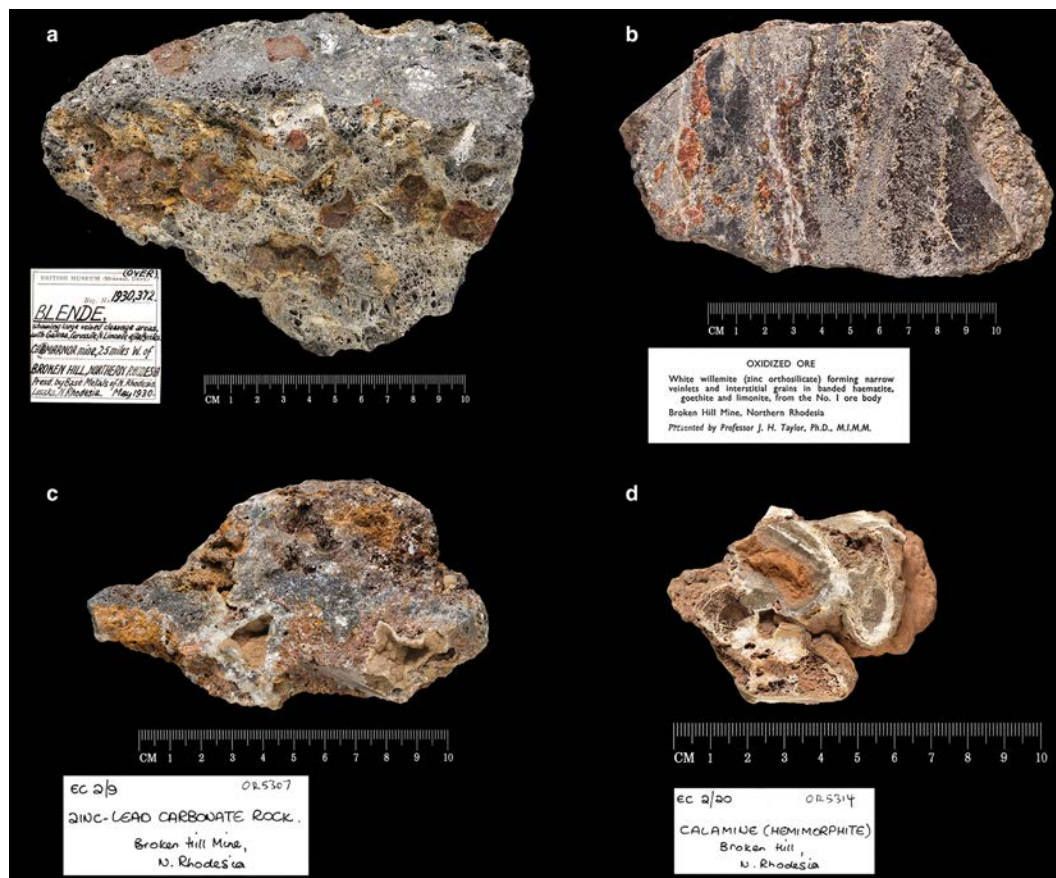
FIG. 2. Examples of Kabwe specimens (NHM ore collection). (*a*) BM1930-372: sphalerite and galena; (*b*) MI29631: silicate Zn ore; (*c*) OR5307: Zn-Pb-carbonate ore; and (*d*) OR5314: 'Calamine' sample: smithsonite and hemimorphite crusts.

willemite formation could have been introduced into the system during silicification of the wallrock dolomite at temperatures >150°C under oxidizing conditions (Kamona and Friedrich, 2007). Kamona and Friedrich (2007) interpreted the first massive willemite generation, replacing the sulfides directly, as hydrothermal, whereas the second generation was supergene. On the contrary, Terracciano (2008) considered a supergene or low-temperature hydro-thermal origin for both willemite generations recognized in the Kabwe deposit.

Materials and methods

For the present study, 16 specimens of Kabwe area ore bodies, housed in the NHM ore collection (Fig. 2, Table 1) were used. To define the ore textural, mineralogical and geochemical character-istics, only a limited number of diverse samples (see Tables 2 and 3) was further selected from the batch of 16 samples. One willemite specimen, belonging to the NHM Mineralogy collection (Table 1), was also used for oxygen isotopic analyses. Sample preparation and analytical methods are described in detail in Appendix 1 (Supplementary material, see below), and are summarized briefly here.

Polished blocks were prepared for optical microscopy (OM), scanning electron microscopy with energy dispersive X-ray spectrometry (SEM-EDS) and automated mineralogy analyses; repre-sentative parts of each sample were ground to produce powder for whole-rock Powder X-ray Diffraction (PXRD) and chemical analyses.

TABLE 1. Specimens of the Kabwe ores used for this study (NHM ore collection).

Specimen (Collection) ID	Specimen ID as used in the text	Specimen description as on the collection label
BM.1907,987	BM1907-987	Lead-zinc-ore
BM.1985,MI29629 1/2	MI29629 1/2	Partly oxidized lead-zinc ore
BM.1985,MI29629 2/2	MI29629 2/2	Partly oxidized lead-zinc ore
BM.1985,MI29631	MI29631	Oxidized ore – No.1 Orebody
BM.1985,MI29633	MI29633	Dolomite
BM.1985,MI32046	MI32046	Sphalerite disseminated in dolomite
OR.5303	OR5303	Vanadium ore (containing descloizite and limonite)
OR.5304	OR5304	Sulfide pre (containing zinc blende, galena and pyrite)
OR.5305	OR5305	Zinc-silicate ore
OR.5307	OR5307	Zinc-lead carbonate ore
OR.5309	OR5309	Zinc-silicate ore
OR.5310	OR5310	Tarbuttite
OR.5312	OR5312	Pyromorphite
OR.5314	OR5314	Calamine (hemimorphite)
BM.1985,MI10900	MI10900	Hemimorphite
BM.1930,372	BM1930-372	Blende showing large veined cleavage areas with galena, cerussite + limonite after pyrite – Carmarnor mine, 2.5 km W of Broken Hill
BM.1920,238*	BM1920-238	Willemite associated with sphalerite

*This specimen is housed in the NHM Mineralogy collection.

The PXRD patterns were obtained using an Enraf Nonius PDS120 diffractometer (NHM), characterized by an asymmetric reflection geometry, with fixed angle between the X-ray tube, the sample surface and the detector. Co$K\alpha$1 radiations were used at 40 kV and 40 mA. The PXRD patterns were analysed using the *Highscore Plus* (Panalytical) software; the PDF4 (Powder Diffraction File from the International Center for Diffraction Data – ICDD) database was used for phase identification. The instrumental configuration adopted and the sample preparation did not permit quantitative phase analysis using the Rietveld method. Mineral abundances were determined as wt.% ranges (Table 2) on the basis of the peak intensity ratio between mineral phases, the modal mineralogy of polished blocks and the whole-rock chemical analyses.

Whole-rock chemical analyses of major and minor elements (see Table 3 for the element list) were carried out at the NHM. Following 4-acid digestion, the sample solutions were analysed by inductively coupled plasma mass spectrometry (ICP-MS) using an Agilent 7700× mass spectrometer. The instrument was calibrated using multi-elements standards (Inorganic Ventures). The limits of quantification were calculated as 10 times the standard deviation of HNO_3 blank solution analysed at least 10 times during the run.

The SEM-EDS analyses were carried out using a ZEISS EVO LS 15 scanning electron microscope (NHM) at 20 kV, with 8.5 mm working distance and 3 nA current mounting with X-Max detectors. Quantitative data sets of selected samples were obtained by wavelength dispersion spectrometry (WDS), using a Cameca SX100 electron microprobe operating at 20 kV, 20 nA and 10 µm spot size (NHM).

The modal mineralogy of the samples was investigated on polished blocks using the 'Mineralogic' system, which is an automated ZEISS EVO•50 SEM, equipped with two Bruker xFlash 5010 EDS detectors. The analyses were carried out with an acceleration voltage of 20 kV, 13 mm working distance and 0.050 s dwell time. The analyses were carried out adopting the 'full map' analytical mode.

The LA-ICP-MS analyses were carried out on an ESI NWR193 UV 193 nm short-pulse-width (<4 ns) laser fitted with a TwoVol2 ablation cell and coupled to an Agilent 7700× quadrupole ICP-MS configured with dual external rotary pumps for

TABLE 2. Semi-quantitative abundances of major minerals in some of the samples analysed (data from PXRD and 'Mineralogic' combined).

	Sphalerite	Galena	Pyrite	Smithsonite	Willemite	Cerussite	Quartz	Hemimorphite	Hydrozincite	Dolomite	Goethite	Hematite	Pyromorphite	Descloizite	Apatite	Tarbuttite
BM1907-987	–	–	–	–	–	xxx	–	xxxx	–	–	x	–	x	–	–	–
BM1930-372	xxxx	x	–	xx	xxx	xx	–	–	–	–	x	x	–	–	–	–
MI29629 1/2	xx	xx	x	xxx	xxx	x	–	–	x	–	x	x	–	–	–	–
MI29629 2/2	x	x	x	xx	xxx	x	–	–	–	–	xxxx	xx	–	–	–	–
MI29631	–	–	–	x	xxxxx	–	–	–	–	–	x	x	x	–	x	–
MI32046	xxx	–	–	xxx	xx	–	–	–	–	–	–	–	–	–	–	–
MI10900	–	–	–	x	–	x	–	xxxx	–	xxx	xx	x	xx	xxx	–	–
OR5305	–	–	–	–	xx	–	xxx	–	–	–	xxxx	x	–	–	–	–
OR5307	–	–	–	xxxxx	–	–	xxx	–	–	–	x	x	–	–	–	–
OR5309	–	–	–	–	xxxx	–	–	–	–	–	Xxx	xxx	–	x	–	–
OR5314	–	–	–	–	–	–	x	xxxx	–	–	x	–	–	–	–	xxxx

– not detected, x: <5 wt.%, xx: 5–20 wt.%, xxx: 20–40 wt.%, xxxx: 40–60 wt.%, xxxxx: >60 wt.%

TABLE 3. Chemical composition of the samples studied.

	wt.%							ppm																						
	Na	Mg	Al	K	Fe	Zn	Pb	V	Cr	Mn	Co	Ni	Cu	Ga	Ge	As	Rb	Sr	Mo	Ag	Cd	In	Sn	Sb	Cs	Ba	Tl	Th	U
Detect. lim.	0.09	0.01	0.03	0.09	0.004	0.001	0.001	1	18	8	1	1	7	0	12	2	1	6	1	1	1	1	4	0	0	4	1	1	1
BM1907-987	<	<	<	<	0.90	31.73	32.19	8	<	92	2	<	80	1	<	13	<	<	3	16	3	<	<	3	0	90	<	<	2
BM1930-372	<	0.17	<	<	0.20	54.05	10.01	7	<	158	<	<	238	21	9	34	<	19	<	11	710	–	–	–	<	53	<	<	39
MI29629 1/2	<	0.14	<	<	3.71	48.17	21.08	57	20	146	5	4	281	7	12	213	<	190	37	48	389	–	–	–	<	15	<	<	39
MI29629 2/2	<	0.10	0.03	<	40.89	22.28	2.16	502	1073	48	7	5	10	3	29	473	<	83	142	2	62	12	21	8	<	12	<	19	180
MI29631	<	0.02	0.04	<	7.66	55.26	0.91	135	<	39	7	5	156	5	18	412	<	10	11	18	19	<	<	29	<	35	<	6	5
MI32046	<	3.17	<	<	0.86	49.47	0.06	33	<	406	12	4	1219	4	13	403	<	20	52	4	395	<	<	12	<	57	<	<	<
OR5305	<	<	<	<	36.82	10.66	3.08	678	<	70	7	11	426	2	<	297	<	153	79	19	7	<	<	6	<	139	<	10	61
OR5307	<	0.24	0.05	<	1.36	54.13	0.65	469	<	75	12	7	99	2	<	63	<	<	4	1	857	<	<	4	0	<	<	6	2
OR5309	<	0.07	0.16	<	37.20	27.68	3.15	5940	83	104	9	8	345	6	17	216	6	6	21	3	8	<	<	31	<	54	<	9	34
OR5314	<	0.04	1.27	0.12	1.00	51.48	1.50	2500	<	1948	7	28	616	5	<	333	13	28	2	19	62	<	<	3	1	59	<	31	5

<, under detection limit; –, not detected.

enhanced sensitivity, located in the LODE laboratory, NHM. Ablated spots were 35–50 µm in diameter, with a fluence of 3.5 J cm^{-2}, fired at a frequency of 10 Hz. The transport gas used was He at a flow rate of 0.5 L min^{-1} mixed with Ar at a flow rate of 1.1 L min^{-1}, in a signal-smoothing device.

The element menus and ICP-MS dwell time settings that were employed to obtain the compositions of the various minerals are listed in Appendix 2 (Supplementary material, see below). Element ratios to an internal standard element (^{29}Si for willemite and hemimorphite, ^{57}Fe for goethite and hematite, and ^{66}Zn for smithsonite, descloizite and sphalerite) were determined by referencing background-corrected integrated intensities from mineral signals to the external calibration standard (see Appendix 1 for details). This was GSD-1g glass (USGS) for goethite and hematite, and NIST 610 for smithsonite and descloizite. Following the procedure in Choulet *et al.* (2017), the external calibration standard for willemite and hemimorphite was NIST 612. More complicated was the analytical approach to the sphalerite analysis and the choice of the appropriate external standard (see Appendix 1 for details). The main limitation of the polymetallic sulfide material MASS-1 as a standard for this work is that Ge is not certified or even included as a reference value, even though Belissont *et al.* (2014) reported a Ge concentration of 57.8 ± 2.6 ppm in the MASS-1 (Dr S. Wilson, pers. comm. in Belissont *et al.*, 2014). For this reason, the external calibration standard for sphalerite was MASS-1 for ^{51}V, ^{53}Cr, ^{55}Mn, ^{57}Fe, ^{59}Co, ^{60}Ni, ^{65}Cu, ^{71}Ga, ^{75}As, ^{95}Mo, ^{107}Ag, ^{111}Cd, ^{115}In, ^{118}Sn, ^{121}Sb, ^{137}Ba, ^{182}W, ^{208}Pb and ^{209}Bi, whereas NIST 610 was used for evaluating the Ge concentration (see Appendices 1 and 2 for details). Note that the Ge value in MASS-1 (as secondary standard), obtained with external calibration by NIST 610 (Table A2 in Appendix 1), was slightly more than twice the amount reported by Belissont *et al.* (2014) as a reference value for MASS-1. Absolute element concentrations were then calculated from internal standard element concentrations (predetermined by SEM-EDS and SEM-WDS) using the program ExLAM (Zachariáš and Wilkinson, 2007). Limits of detection were set at the conventional 3σ of the background signal variation (Longerich *et al.*, 1996). GSD-1g, NIST 612, or NIST 610 were used as secondary standards; NIST 2782 and BC_28 (the in-house magnetite standard of Dare *et al.*, 2014) were also monitored during Fe oxide or oxy-hydroxide analysis. Time-resolved raw counts-per-second signals were screened meticulously and the

longest 'clean' integration intervals possible (up to 60 s of signal) were retained.

Carbon and oxygen isotope analyses were performed on smithsonite and cerussite. Hand-picked carbonate mineral specimens were analysed at SUERC (East Kilbride, Scotland) on an Analytical Precision AP2003 mass spectrometer equipped with a separate acid injector system, after reaction with 105% H$_3$PO$_4$ under He atmosphere at 70°C. Isotopic results are reported using the conventional δ‰ notation. Mean analytical reproducibility, based on replicates of the SUERC laboratory standard MAB-2 (Carrara Marble), was ~±0.2‰ for both carbon and oxygen. The δ^{13}C data are reported relative to V-PDB (Vienna pee dee belemnite), whereas the δ^{18}O values of carbonates are quoted relative to V-SMOW (Vienna standard mean ocean water).

The oxygen isotopic composition of willemite was analysed on hand-picked crystals, using a laser fluorination procedure, involving total sample reaction with excess ClF$_3$ using a CO$_2$ laser as a heat source (>1500°C; following Sharp, 1990). All combustions resulted in 100% release of O$_2$ from the silica lattice. This O$_2$ was then converted to CO$_2$ by reaction with hot graphite, then analysed on-line by a VG Isotech SIRA II spectrometer. Reproducibility is better than ±0.3‰ (1σ), based on repeat analyses of international and internal lab standards run during these analyses. Results are reported in standard notation (δ^{18}O) as per mil (‰) deviations from V-SMOW standard.

Results

Mineralogy, petrography and chemistry of the ores

The mineralogical and chemical bulk compositions of the samples analysed are reported in Tables 2 and 3. Samples MI32046, MI129629 1/2, MI129629 2/2 and BM1930-372 contain sulfide minerals (sphalerite, galena and pyrite), together with oxidized phases (willemite, smithsonite, cerussite and hematite) (Fig. 3). Other samples instead consist only of oxidized minerals, mostly represented by willemite, smithsonite and hemimorphite (Table 2) (Fig. 3).

From the ore textures observed, it is possible to recognize a primary galena generation (G1) interstitial to sphalerite (Fig. 4*a*). G1 is almost pure, whereas sphalerite can contain up to 0.9 wt.% Fe. Renierite is included locally in sphalerite
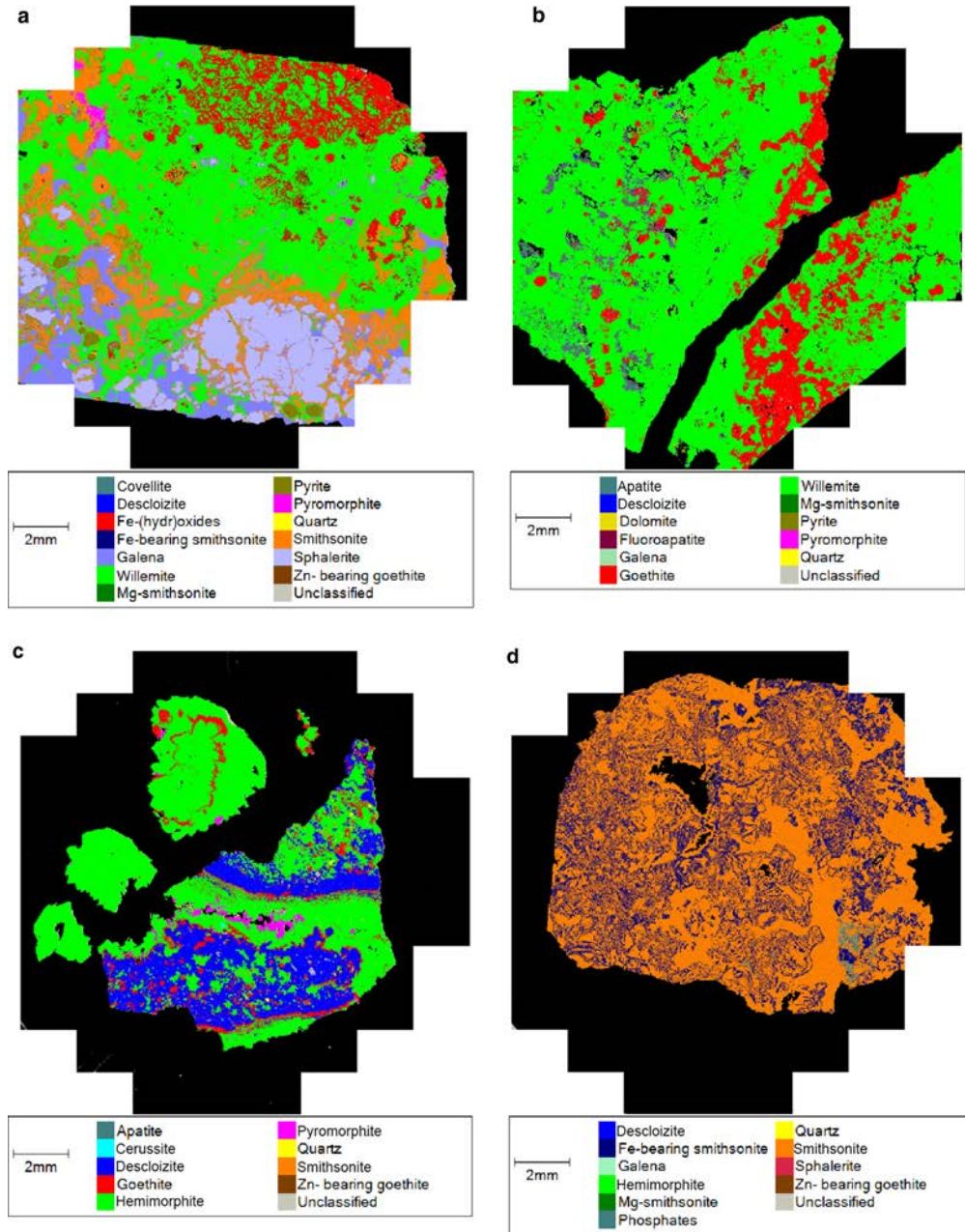
FIG. 3. Examples of modal mineralogical analyses using 'Mineralogic' from Zeiss. (*a*) MI29629 2/2: sulfides replaced by willemite 1; (*b*) MI29631: willemite 2 overprinted by goethite; (*c*) MI10900: concretionary agglomerate of descloizite, hemimorphite and pyromorphite; and (*d*) OR5307: smithsonite-rich specimen.

(Fig. 4*b*). Pyrite is disseminated between the sphalerite and galena (Fig. 4*c*). This mineral association is overprinted by at least three different mineral assemblages. The first assemblage consists of a first generation of massive microcrystalline willemite (W1) replacing directly sphalerite and the

FIG. 4. Optical microscopy - reflected light: (*a*) OR5304: primary sulfides assemblage: sphalerite (Sph) with interstitial galena 1 (G1); (*b*) MI29629 1/2: sphalerite, containing a Ge-sulfide inclusion, replaced by willemite 1 (W1); the reaction boundary between sphalerite and willemite is marked by a thin layer of galena 2 (G2); (*c*) MI29629 2/2: pyrite (Py), sphalerite and galena 1 remnants after willemite 1 replacement; and (*d*) MI29629 2/2: willemite 1 directly replacing galena 1.
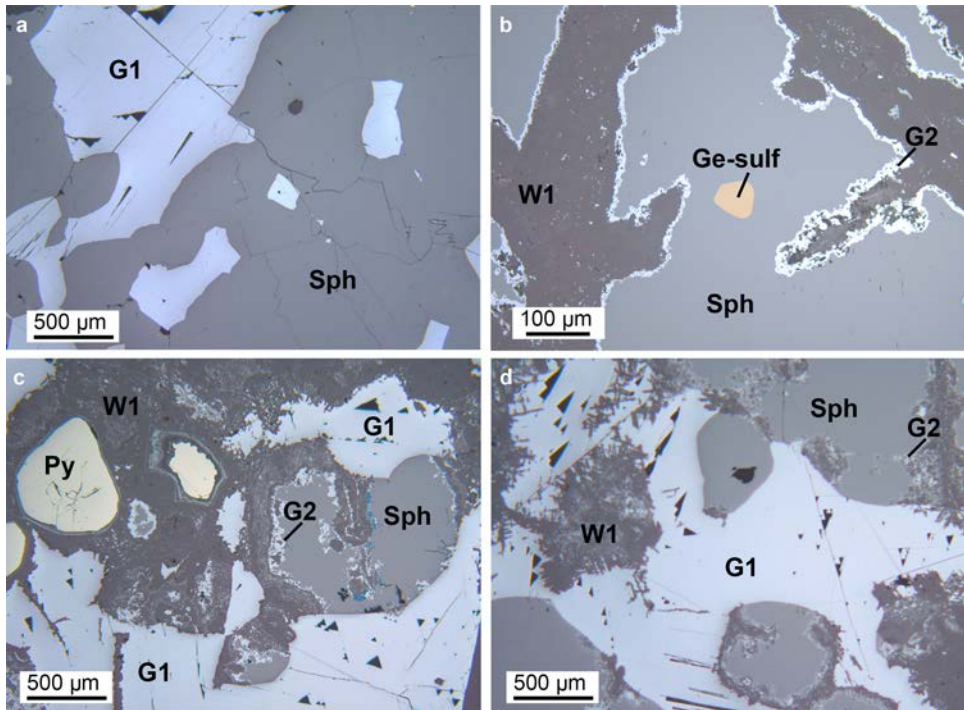
interstitial galena (Fig. 4*d*). At the reaction boundaries with the Zn-silicate, sphalerite remnants are always rimmed by thin layers of a second galena generation (G2) and covellite (Fig. 4*b*). Other galena microdomains are finely dispersed within the massive W1, and can be associated locally with tiny Ag-sulfide inclusions. W1 seems to have been mostly developed along the fractures and the open spaces originally occurring in the sulfide association, and does not contain major elements in its structure. The second assemblage consists of a second willemite generation (W2), which is developed in well formed crystals of variable size (in some cases 0.5 mm hexagonal crystals in geodes) (Fig. 5*a*). W2 is zoned chemically, with alternating Pb-rich (up to 2 wt.% Pb) and Pb-poor bands (Fig. 5*b*). A third assemblage is formed by (Fig. 5*c*, *d*): smithsonite, cerussite, hemimorphite, sauconite, covellite, Fe-oxyhydroxides, pyromorphite, vanadinite, descloizite, mottramite, apatite, mimetite and tarbuttite. Smithsonite and hemimorphite

replace willemite W1 and sphalerite directly (Fig. 5*c*), and also form euhedral crystals in cavities (Fig. 5*d*). At the reaction boundaries between sphalerite and smithsonite, covellite is observed commonly (Fig. 4*c*). Agglomerates of prismatic covellite crystals also occur in cavities within sphalerite remnants. Cerussite replaces galena directly (Fig. 5*c*). Zinc and Pb carbonates are commonly associated with goethite and hematite, which can also replace willemite directly (Fig. 6*a*). Hemimorphite presents two different textures: a crustiform texture (Fig. 6*b*), where hemimorphite crusts alternate with smithsonite crusts, and a typical crystalline texture of fan-shaped agglomerates of euhedral tabular crystals (Fig. 6*c*). Smithsonite crusts are commonly Mg-rich (up to 2 wt.% Mg). Minerals like pyromorphite and tarbuttite commonly fill voids between the euhedral hemimorphite (Fig. 6*c*,*d*). None of the oxidized minerals (silicates, carbonates and vanadates) show any signs of deformation.

By correlating the mineralogy of the samples (Table 2) with whole-rock chemical compositions (Table 3), it is possible to see that largest amounts of Fe correspond to Fe-oxyhydroxide occurrences, the largest amounts of Zn coincide with sphalerite- and willemite-bearing samples, whilst Pb is associated with galena and cerussite occurrences. The critical element, Ge, is above the detection limits in willemite- and Fe-oxyhydroxide-bearing samples and in specimens containing sphalerite. Gallium reaches tens of ppm (21 ppm) only in sample BM1930-372, which contains sphalerite and willemite. The indium concentration is above minimum detection limits only in sample MI29631, which consists largely of willemite and minor goethite. Other trace elements with significant concentrations (Table 3) are V (typically associated with vanadates), Cr (1073 ppm in a goethite-rich sample), Mn, Cu and As (hundreds of ppm in samples containing sulfides, willemite and Fe-oxyhydroxides). Cadmium reaches concentrations well above 300 ppm in samples consisting of sphalerite and smithsonite. Molybdenum and U levels are ~100 ppm in samples containing Fe-oxyhydroxides. The tarbuttite-bearing sample (OR5314) is characterized by large Mn, Cu and As contents.

Chemical compositions of mineral phases

The LA-ICP-MS analyses were carried out on sphalerite, W1 and W2, hemimorphite, hematite, goethite, smithsonite and descloizite. The mean compositions of the most abundant elements revealed in the minerals analysed are given here. In Tables 4–10, maximum, minimum and median values are also reported. Zonation was registered only in willemite (Pb-zoning), whilst the other minerals analysed were remarkably unzoned.

In two analysed samples, BM1930-372 and MI29629 2/2 (Table 4), sphalerite contains minor amounts of Fe (mean 1177 and 3759 ppm), and minor to trace amounts of Cd (mean 970 and 1038 ppm), whereas all the other elements are scarce.

Willemite W1, analysed in samples BM1930-372 and MI29629 1/2 (Table 5), was found to contain discrete trace (hundreds of ppm or less) amounts of B (mean 92 and 118 ppm), Ca (mean 58 and 59 ppm) and Cd (mean 61 and 40 ppm). In the samples of W1 analysed, both As and Ge contents are variable; respective means are 8 and

586 ppm for As and 3 and 30 ppm for Ge. W1 locally has high Pb values, related to the occurrence of G2 micro-inclusions. W2 shows a chemical zoning as stated before, with alternating Pb-rich (up to 2 wt.% Pb) and Pb-poor bands. W2 was analysed by LA-ICP-MS in two samples, OR5309 and MI29631 (Table 5), where it was found to contain similar amounts of Ca and Cd as observed in W1, with minor Ge (mean 22 and 47 ppm) and Cu (mean 4 and 30 ppm), but apparently no B. W2 Pb-rich bands generally contain more Ge, As, Ca and Mg than the Pb-poor bands.

Hemimorphite was analysed in three samples: MI10900, OR5314 and BM1907-987 (Table 6). In these samples hemimorphite appears to have a variable trace-element composition. In sample OR5314, where hemimorphite is associated with tarbuttite, vanadium has elevated values (mean 247 ppm V). This hemimorphite also contains significant Cu (mean 92 ppm) and Cd (mean 41 ppm). In the sample MI10900, hemimorphite is associated with descloizite, and it contains significant Pb (mean 723 ppm), Cd and Cu (mean 123 ppm Cd, 61 ppm Cu), but apparently no V. In sample BM1907-987 hemimorphite is associated with cerussite, and only contains traces of Pb (mean 104 ppm). No Ge has been detected in this Zn hydro-silicate.

Goethite and hematite have been analysed in six samples (Tables 7 and 8): BM1930-372, MI29631, OR5305, OR5309, MI10900 and MI29629 2/2. Fe-oxyhydroxides contain major (~1 wt.%) amounts of Zn, Si and Pb, and minor amounts of Al. Goethite is shown to be richer in Zn than hematite. Goethite and hematite contain hundreds of ppm of several metals (Ti, V, Cr, Mn, Co, Ni, Cu, Ge, As, Y, Mo, Cd, In, Sb, W and U), variously distributed in these minerals in the analysed samples, yet Ge appears to be very low (Tables 7 and 8). In both these Fe minerals, significant Ga was only found in sample BM1930-372 (max 138 ppm). The indium content is high in sample MI29631 (max 46 ppm in goethite and 60 ppm in hematite).

The smithsonite trace-element composition was evaluated in sample BM1930-372 (Table 9). This Zn-carbonate contains major amounts of Mg (mean ~2 wt.%), and traces of Fe, Cd and Pb. Descloizite contains trace amounts of Ca, Cu and As (mean values in sample OR5303 of 726 ppm Ca, 2475 ppm Cu and 936 ppm As; Table 10). No Ge, In or Ga was detected in the smithsonite and descloizite analysed.
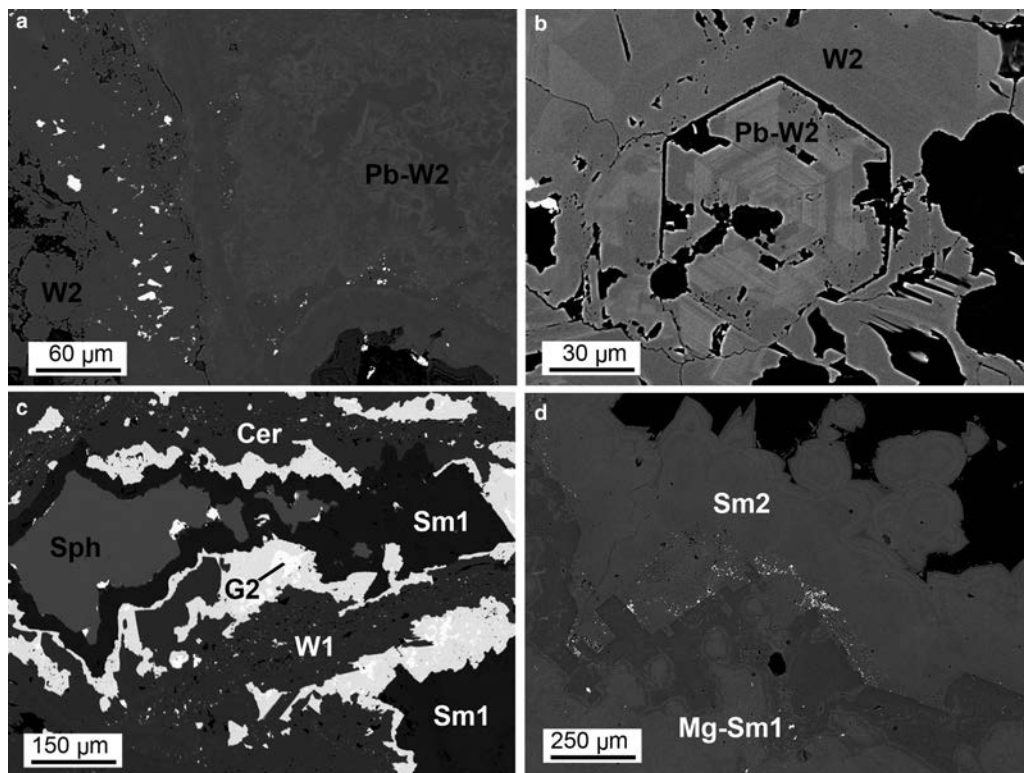
Fig. 5. Backscattered electron (BSE) images of replacement textures: (*a*) MI29629 2/2: concretionary agglomerate of willemite 2 (W2), with alternating Pb-poor and Pb-rich layers; (*b*) OR5309: hexagonal prismatic crystal of willemite 2, characterized by oscillatory chemical zoning; (*c*) BM1930-372: an original aggregate of sphalerite (Sph) and galena 2 (G2) replaced by carbonates: galena 2 is replaced by cerussite (Cer) and sphalerite is replaced by smithsonite; and (*d*) OR5307: smithsonite, locally bearing Mg, forming botryoidal crust (Sm2) and replacing dolomite crystals of the host rock (Sm1).

Stable isotope geochemistry

Oxygen isotope compositions have been determined for both W1 and W2 (Table 11), smithsonite (replacing sphalerite and crystals in geodes), and cerussite (replacing galena) (Table 12). W1 yields $\delta^{18}O$ compositions of between 13.9 and 15.7‰, with a mean value of $14.7 \pm 0.9‰$ (1σ; $n = 5$). In marked contrast, W2 is characterized by negative $\delta^{18}O$ values, ranging between −4.6‰ and −0.3‰, with a mean value of $-2.7 \pm 1.5‰$ (1σ; $n = 6$). $\delta^{18}O$ compositions of smithsonite that has replaced sphalerite, and smithsonite crystals are similar and range between 20.9‰ and 22.8‰ (all carbonate O isotope data discussed *vs*. the V-SMOW standard), whereas the single measurement from cerussite has a $\delta^{18}O$ of 13.1‰. By using the cerussite-water and smithsonite-water oxygen isotope fractionation equations of Gilg *et al.*

(2008), and the willemite-water oxygen isotope fractionation equation of Zheng (1993):

$$1000 \ln \alpha_{\text{cerussite-water}} = 2.29(10^6/T^2) - 3.56;$$
$$1000 \ln \alpha_{\text{smithsonite-water}} = 3.10(10^6/T^2) - 3.50;$$
$$1000 \ln \alpha_{\text{willemite-water}} = 3.79(10^6/T^2)$$
$$- 8.94(10^3/T) + 2.50;$$

it is possible to plot the $\delta^{18}O$ values of the analysed phases in a temperature *vs*. water $\delta^{18}O$ composition diagram (Fig. 7). Willemite W1 and smithsonite paths can be seen to cross at more than 300°C and more than 15‰ fluid $\delta^{18}O$ (Fig. 7*a*), whereas smithsonite and cerussite paths cross at ∼30°C and ∼−8‰ fluid $\delta^{18}O$ (Fig. 7*b*). W2 does not cross any W1, cerussite or smithsonite path. $\delta^{13}C$ compositions of smithsonite and cerussite are always negative, ranging from −11.1 to −3.6‰.
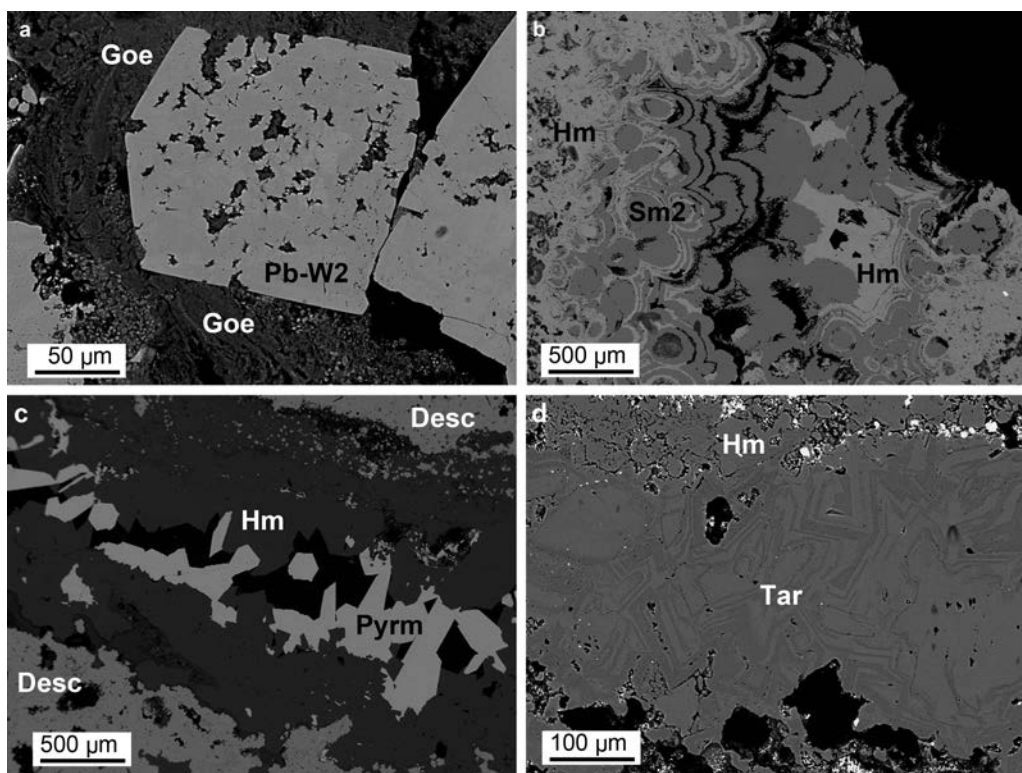
FIG. 6. Back-scattered electron (BSE) images of typical supergene minerals: (*a*) MI29631: goethite (Goe) altering a Pb-bearing willemite 2 (Pb-W2) crystal; (*b*) OR5314: alternating crusts of hemimorphite (Hm) and smithsonite 2 (Sm2); (*c*) MI10900: hemimorphite platy crystals in a cavity, followed by pyromorphite (Pyrm) crystals; and (*d*) OR5314: tarbuttite (Tar) vein in hemimorphite. Desc = descloizite.

Discussion

Mineral paragenesis and genetic processes

The petrography conducted on the selected specimens from the NHM ore collection confirmed the complex paragenesis reported in previous studies (Kamona, 1993; Kamona and Friedrich, 2007; Terracciano, 2008). In agreement with the previous studies, two willemite generations were recognized: the first directly replaces the sulfides, and a second leading to well formed crystals in cavities. We also find that these two willemite phases were followed paragenetically by minerals consistent with a supergene alteration assemblage. Unlike previous studies (i.e. Kamona and Friedrich, 2007; Terracciano, 2008), we have found no evidence in our sample suite that W2 is co-genetic with the minerals typically recognized as supergene (e.g. goethite, hematite and smithsonite). In fact, all the textures identified in the samples analysed, even

though compatible with a coeval precipitation of W2 with Zn-Pb-carbonates, Fe-oxyhydroxides and vanadates, were probably the result of an 'over-printing' process, where smithsonite, cerussite, hemimorphite, goethite, hematite, descloizite, etc., formed together, almost at the same time, 'above' and 'in the spaces between' pre-existing minerals (i.e. the sulfides and the two willemite phases). For this reason, in the paragenetic scheme represented in Fig. 8, we suggest that the original sulfide association was altered by at least three oxidation stages: two stages that were dominated by the formation of willemite, and another characterized by weathering-related processes. The existence of these three stages is also evident when looking at the stable oxygen isotopes. When plotting the mineral-water equilibrium curves in a temperature *vs.* water $\delta^{18}O$ diagram (Fig. 7), the paths of co-genetic minerals cross at points indicating their precipitation temperature and the $\delta^{18}O$ composition

TABLE 4. Major (WDS) and trace (LA-ICP-MS) element composition of sphalerite.

Sample	S	Mn	Fe	Zn	Pb	Cd	Mn	Fe	Cu	Ga	Ge*	Cd	In	Sn
	wt.%						ppm							
MI29629 2/2 (n = 19)														
Mean	32.59	0.03	0.94	66.86	0.10	0.12	170.28	3759.43	6.61	0.08	5.72	970.26	0.003	0.76
Stand. Dev.	0.40	0.00	0.01	0.12	0.01	0.02	8.44	98.94	5.17	0.02	6.51	36.22	0.001	0.11
Maximum	33.43	0.04	0.95	67.05	0.12	0.17	189.36	3960.09	26.44	0.12	31.19	1026.22	0.006	1.06
Minimum	31.86	0.03	0.92	66.62	0.09	0.10	156.86	3583.80	3.13	0.06	1.95	898.98	0.001	0.58
Median	32.53	0.03	0.94	66.90	0.11	0.12	170.39	3759.29	5.80	0.08	5.23	965.99	0.003	0.75
Det. Lim.	0.04	0.03	0.02	0.04	0.09	0.09	0.13	1.57	0.10	0.01	0.28	0.54	0.001	0.27
BM1930-372 (n = 15)														
Mean	32.09	0.03	0.30	67.70	0.10	0.14	206.03	1177.14	17.55	14.66	1.05	1038.09	0.500	3.75
Stand. Dev.	0.51	0.00	0.01	0.11	0.01	0.02	5.62	26.13	0.45	0.25	0.19	12.34	0.013	0.43
Maximum	33.18	0.04	0.32	67.92	0.11	0.18	215.30	1227.06	18.35	15.02	1.49	1057.86	0.523	4.40
Minimum	31.01	0.03	0.26	67.36	0.09	0.10	195.23	1140.70	16.75	14.21	0.83	1016.96	0.485	3.11
Median	32.09	0.03	0.30	67.70	0.10	0.14	205.93	1179.45	17.58	14.67	1.00	1042.13	0.503	3.78
Det. Lim.	0.04	0.03	0.02	0.04	0.09	0.09	0.14	1.68	0.08	0.01	0.27	0.51	0.005	0.27

LA-ICP-MS analyses: Internal standard = Zn; External standard = MASS-1. *External standard for Ge = NIST 610.
Stand. Dev. — standard deviation; Det. Lim. — detection limit.

14

TABLE 5. Major (EDS) and trace (LA-ICP-MS) element composition of willemite.

Mineral phase Sample	Si	Zn	Pb	B	Mg	Al	Ca	V	Mn	Fe	Cu	Ga	Ge	As	Sr	Ag	Cd	In	Pb
	wt.%			ppm															
Willemite 1																			
BM1930-372 (n = 22)																			
Mean	12.78	60.15	–	92.34	4.93	2.64	57.94	8.90	3.65	13.74	1.92	13.83	2.87	8.48	0.16	1.83	60.88	0.70	1213.16
Stand. Dev.	0.20	0.54	–	109.11	17.26	2.77	4.97	8.97	4.82	12.73	3.67	7.52	3.21	9.13	0.33	2.24	15.11	0.74	1375.20
Maximum	13.07	61.33	0.59	569.70	82.06	12.55	64.60	36.23	18.26	48.69	13.90	28.29	13.34	32.40	1.17	8.33	94.71	3.17	5173.35
Minimum	12.35	59.10	0.59	30.21	0.25	0.81	51.10	1.04	0.19	2.72	0.20	3.08	0.92	0.33	0.008	0.70	39.65	0.02	179.23
Median	12.86	60.22	–	70.90	0.96	1.45	58.10	6.10	1.78	8.76	0.43	12.17	1.81	4.39	0.04	0.83	57.54	0.41	782.59
Det. Lim.	0.02	0.05	0.05	1.50	0.22	0.76	50.69	0.02	0.18	3.84	0.07	0.02	0.47	0.32	0.005	0.02	0.74	0.003	0.06
MI29629 1/2 (n = 13)																			
Mean	12.56	60.12	–	118.30	1.83	12.96	58.65	3.24	0.71	15.09	1.45	0.08	29.81	586.05	0.10	1.09	39.60	0.004	1484.09
Stand. Dev.	0.15	0.67	–	47.60	1.27	18.78	9.91	2.84	0.82	15.03	1.86	0.06	12.89	290.90	0.07	0.69	15.03	0.001	1352.78
Maximum	12.79	61.38	0.65	215.36	4.40	59.91	75.06	7.96	3.29	43.87	6.85	0.19	47.23	1142.38	0.28	2.35	77.73	0.007	4691.51
Minimum	12.33	59.37	0.65	19.66	0.20	1.88	45.70	0.05	0.23	2.25	0.13	0.03	8.47	24.66	0.03	0.47	21.31	0.003	374.69
Median	12.51	60.17	–	118.20	2.04	4.81	58.20	2.87	0.40	5.05	0.91	0.06	31.50	540.38	0.10	0.74	39.39	0.004	929.59
Det. Lim.	0.02	0.05	0.05	1.48	0.19	1.15	45.13	0.02	0.15	3.22	0.05	0.02	0.37	0.30	0.01	0.01	0.53	0.003	0.06
Willemite 2																			
OR5309 (n = 29)																			
Mean	12.58	59.64	0.87	1.51	8.94	5.73	50.21	6.97	0.44	10.45	3.80	0.24	46.77	316.95	0.03	0.87	70.82	–	4038.55
Stand. Dev.	0.18	0.85	0.50	0.42	8.22	4.21	4.90	7.77	0.28	11.43	3.58	0.30	22.28	87.97	0.02	0.25	23.17	–	2277.01
Maximum	12.93	60.96	2.15	2.60	26.77	16.52	64.80	35.46	1.22	45.94	16.79	1.46	91.36	535.90	0.08	1.71	126.52	<	7945.38
Minimum	12.21	57.54	0.06	0.92	0.15	0.82	42.50	1.07	0.15	3.36	0.71	0.04	5.00	169.89	0.01	0.60	29.52	–	916.74
Median	12.55	59.88	0.90	1.44	7.09	4.99	49.64	5.02	0.41	5.90	2.39	0.14	46.88	306.91	0.02	0.81	66.19	–	4078.66
Det. Lim.	0.02	0.05	0.05	1.26	0.20	0.64	41.20	0.02	0.15	3.27	0.05	0.01	0.39	0.30	0.005	0.01	0.51	0.003	0.07
MI29631 (n = 22)																			
Mean	12.68	59.96	1.96	2.30	10.84	6.28	111.63	0.54	1.44	18.22	29.75	0.60	21.50	251.82	1.87	1.18	43.80	2.61	7352.58
Stand. Dev.	0.13	0.65	0.06	0.47	4.99	5.09	93.77	0.50	1.10	15.83	23.28	1.12	13.46	84.36	2.14	0.95	12.54	1.43	4105.46
Maximum	13.02	61.22	2.01	3.58	19.33	19.49	349.28	1.91	4.48	68.28	78.99	4.60	49.89	476.97	7.82	4.75	72.23	5.85	15526.17
Minimum	12.52	58.84	1.90	1.74	3.92	1.74	24.00	0.11	0.33	2.90	0.59	0.03	2.19	118.42	0.06	0.56	24.42	0.27	1009.43
Median	12.66	59.79	1.96	2.23	9.03	4.16	89.05	0.24	0.99	13.06	21.88	0.13	18.57	246.54	1.13	0.81	42.85	2.12	7399.14
Det. Lim.	0.02	0.05	0.05	1.71	0.06	0.25	20.53	0.01	0.09	1.29	0.04	0.01	0.16	0.16	0.002	0.01	0.41	0.002	0.03

–: not evaluated; <: less than the detection limit; LA-ICP-MS analyses: Internal standard = Si; External standard, LODE_NIST 612.
Stand. Dev. — standard deviation; Det. Lim. — detection limit.

TABLE 6. Major (EDS) and trace (LA-ICP-MS) element composition of hemimorphite.

Sample	Si	Zn	B	Mg	Al	K	Ca	V	Mn	Fe	Cu	Ga	Ge	As	Ag	Cd	In	Pb
	wt.%							ppm										
MI10900 (*n* = 24)																		
Mean	11.63	55.01	3.39	0.15	12.50	–	–	0.03	0.27	6.64	60.65	0.02	3.06	1.50	0.92	122.77	0.003	723.09
Stand. Dev.	0.21	0.58	1.95	0.19	8.74	–	–	0.04	0.24	5.58	63.20	0.02	1.92	1.07	0.36	53.67	0.001	623.25
Maximum	11.89	55.99	8.34	0.67	29.64	<	<	0.12	0.66	20.31	181.77	0.07	7.48	5.08	1.88	218.75	0.005	1906.81
Minimum	11.16	54.14	1.43	0.04	0.50	–	–	0.01	0.05	0.86	0.26	0.01	0.55	0.26	0.55	61.62	0.002	1.90
Median	11.66	54.89	2.78	0.08	11.42	–	–	0.01	0.14	5.36	40.16	0.02	2.61	1.10	0.80	101.20	0.003	595.88
Det. Lim.	0.02	0.05	1.11	0.04	0.15	1.30	13.67	0.01	0.06	1.28	0.02	0.00	0.10	0.10	0.01	0.22	0.001	0.02
OR5314 (*n* = 14)																		
Mean	11.88	56.50	7.87	5.52	56.74	13.31	58.25	246.80	0.59	18.13	91.72	0.03	1.86	21.61	5.86	40.79	0.003	3.66
Stand. Dev.	0.24	0.73	2.95	5.29	74.81	12.38	56.39	245.76	0.63	13.60	69.37	0.04	0.61	10.78	9.48	16.48	0.001	4.60
Maximum	12.17	57.52	12.82	19.76	233.94	30.48	183.61	853.15	1.70	44.75	248.59	0.14	2.75	36.98	36.67	87.92	0.004	17.50
Minimum	11.45	54.69	3.88	0.35	1.80	1.81	16.77	10.92	0.07	6.39	28.24	0.01	0.65	6.60	0.63	24.84	0.002	0.31
Median	11.90	56.66	7.25	4.24	18.80	6.40	45.53	203.38	0.30	12.34	87.21	0.02	2.03	19.73	2.21	35.64	0.003	2.23
Det. Lim.	0.02	0.05	1.04	0.06	0.25	1.92	16.18	0.01	0.09	1.76	0.03	0.01	0.15	0.12	0.01	0.27	0.002	0.02
BM1907-987 (*n* = 13)																		
Mean	11.91	56.65	11.35	0.27	12.76	–	–	0.06	0.08	3.46	5.09	0.01	3.72	1.69	0.72	25.49	0.003	104.47
Stand. Dev.	0.26	1.82	10.76	0.20	9.34	–	–	0.05	0.01	3.21	4.38	0.01	2.60	1.21	0.17	5.55	0.000	169.10
Maximum	12.16	58.50	30.08	0.66	29.45	<	<	0.16	0.10	7.08	13.35	0.02	9.23	3.72	1.13	37.38	0.004	571.99
Minimum	11.47	53.54	1.48	0.07	1.60	–	–	0.02	0.07	0.96	0.98	0.00	0.29	0.45	0.54	18.30	0.002	15.60
Median	12.01	57.20	6.59	0.28	11.14	–	–	0.04	0.08	2.35	2.54	0.01	2.87	1.23	0.66	25.05	0.003	37.02
Det. Lim.	0.02	0.05	0.93	0.05	0.21	1.67	17.63	0.01	0.08	1.52	0.03	0.01	0.12	0.10	0.01	0.17	0.002	0.01

–: not evaluated; <: less than the detection limit; LA-ICP-MS analyses: Internal standard = Si; External standard = LODE_NIST 612.
Stand. Dev. — standard deviation; Det. Lim. — detection limit.

TABLE 7. Major (EDS) and trace (LA-ICP-MS) element composition of goethite.

Sample	Al	Si	P	Fe	Zn	Pb	Ti	V	Cr	Mn	Co	Ni	Cu	Ga	Ge	As	Y	Mo	Cd	In	Sb	W	U
	wt.%						ppm																
BM1930-372 (n = 8)																							
Mean	–	1.17	–	55.63	2.31	3.35	0.55	62.59	2.77	27.38	1.08	7.06	66.96	30.24	6.21	163.54	1.01	329.71	5.20	0.13	35.87	144.12	22.92
Stand. Dev.	–	0.38	–	1.03	0.62	3.16	0.22	71.80	0.87	37.32	0.87	4.62	41.67	45.51	3.73	151.84	0.19	479.97	1.74	0.24	60.21	234.10	16.51
Maximum	<	1.70	<	57.35	3.32	6.90	0.85	195.57	3.78	89.44	2.44	13.66	153.42	138.17	11.86	499.61	1.26	1331.82	8.89	0.68	150.09	649.60	54.29
Minimum	–	0.80	–	54.08	1.36	0.54	0.35	3.37	1.53	5.16	0.23	1.83	12.94	4.10	1.91	64.14	0.75	20.34	2.75	0.01	1.83	1.47	10.81
Median	–	0.98	–	55.59	2.33	1.82	0.51	26.00	2.79	8.22	0.92	7.86	58.92	12.65	5.61	92.35	1.08	121.87	4.91	0.02	4.40	34.81	15.58
Det. Lim.	0.05	0.05	0.02	0.05	0.05	0.05	0.37	0.04	1.38	0.33	0.02	0.17	0.13	0.02	0.58	0.41	0.01	0.02	0.40	0.01	0.09	0.02	0.01
MI29631 (n = 25)																							
Mean	0.49	1.47	–	56.04	1.63	2.91	36.32	78.41	15.09	187.17	68.93	47.12	260.93	10.19	2.15	182.60	1.55	35.86	10.36	17.39	131.96	12.87	17.97
Stand. Dev.	0.19	0.25	–	1.76	0.46	0.64	33.64	25.13	11.52	55.60	22.11	19.39	294.24	6.06	1.02	62.35	0.59	19.20	2.27	8.98	45.67	7.26	10.82
Maximum	0.63	1.91	<	57.98	2.79	4.13	124.32	127.93	45.90	326.77	117.05	107.22	1391.10	36.75	5.09	336.17	3.13	64.42	17.59	46.43	242.11	29.14	38.11
Minimum	0.27	0.91	–	50.35	0.91	2.04	5.26	24.84	3.14	90.46	22.98	28.49	130.56	5.85	0.78	81.21	0.54	9.22	6.60	5.16	53.04	2.14	1.75
Median	0.57	1.41	–	56.29	1.57	2.90	21.20	83.76	11.06	194.71	69.73	39.05	172.81	8.42	2.04	180.16	1.63	35.43	9.91	13.03	138.19	14.05	18.29
Det. Lim.	0.05	0.05	0.02	0.05	0.05	0.05	0.23	0.02	0.62	0.17	0.01	0.08	0.06	0.01	0.29	0.21	0.003	0.01	0.19	0.01	0.04	0.01	0.004
OR5305 (n = 8)																							
Mean	–	1.74	–	53.64	2.26	2.62	0.60	139.69	9.37	35.96	61.95	35.62	50.87	1.73	1.46	127.29	0.23	46.37	40.97	0.009	4.82	8.47	33.51
Stand. Dev.	–	0.13	–	0.42	0.84	0.46	0.38	79.16	14.65	15.87	14.77	6.37	19.94	0.64	0.41	48.74	0.08	17.62	22.52	0.002	2.74	4.60	14.56
Maximum	<	1.90	<	54.28	3.09	3.43	0.87	265.86	37.32	60.89	86.72	41.85	72.49	2.99	1.86	186.20	0.36	72.05	77.21	0.013	10.01	14.45	9.65
Minimum	<	1.53	–	53.17	0.87	2.10	0.33	11.22	0.91	8.37	43.08	25.20	16.45	1.03	0.66	27.01	0.10	14.75	19.43	0.007	1.20	0.50	9.01
Median	–	1.76	–	53.62	2.54	2.47	0.60	128.64	1.87	40.65	65.14	36.39	58.96	1.69	1.61	132.35	0.23	50.54	36.20	0.008	4.51	8.88	35.31
Det. Lim.	0.05	0.05	0.02	0.05	0.05	0.05	0.27	0.02	0.64	0.19	0.01	0.10	0.06	0.01	0.32	0.23	0.003	0.01	0.22	0.006	0.04	0.01	0.01
OR5309 (n = 7)																							
Mean	0.67	0.99	–	51.68	3.22	0.87	232.80	107.23	217.98	52.17	4.69	12.28	120.75	19.89	3.67	242.99	4.10	21.49	8.75	0.26	69.59	10.71	43.58
Stand. Dev.	0.12	0.17	–	0.71	0.85	0.12	67.90	76.77	156.59	4.19	3.04	2.70	31.70	3.07	0.50	89.50	0.68	9.14	3.61	0.04	14.22	1.84	26.18
Maximum	0.82	1.32	<	52.44	4.94	1.01	329.79	271.40	527.44	56.73	10.50	16.81	167.26	23.81	4.72	406.27	5.23	33.05	14.65	0.32	92.09	12.91	98.03
Minimum	0.51	0.83	–	50.78	2.33	0.69	139.21	58.26	34.16	44.54	2.01	10.42	78.69	15.60	3.12	149.33	3.38	10.75	4.98	0.20	51.98	8.00	27.18
Median	0.71	0.97	–	51.89	3.06	0.89	236.71	76.22	212.69	53.13	4.10	10.84	124.75	20.64	3.55	210.37	4.11	19.61	8.73	0.28	68.10	10.99	30.78
Det. Lim.	0.05	0.05	0.02	0.05	0.05	0.05	0.28	0.03	0.90	0.24	0.01	0.11	0.09	0.02	0.38	0.32	0.005	0.02	0.33	0.01	0.06	0.03	0.01
MI10900 (n = 11)																							
Mean	0.20	1.86	0.33	47.31	6.29	3.03	0.19	26.16	9.85	30.22	0.63	3.29	2178.84	5.02	5.19	211.19	17.31	28.89	44.29	–	5.50	5.62	17.87
Stand. Dev.	0.09	0.15	0.08	1.06	1.27	0.12	0.03	1.11	1.07	13.58	0.02	0.27	164.24	0.33	0.68	38.54	1.03	4.44	4.81	–	0.83	0.57	0.69
Maximum	0.30	2.26	0.55	49.34	8.72	3.32	0.24	27.92	11.41	57.22	0.66	3.91	2515.92	5.35	6.50	285.00	18.72	36.21	53.97	<	7.30	6.23	19.32
Minimum	0.10	1.39	0.10	45.73	4.91	2.72	0.16	24.44	8.05	17.48	0.59	3.05	1960.56	4.31	4.25	153.60	15.86	23.41	37.66	–	4.49	4.70	16.76
Median	0.24	1.93	0.37	47.29	5.81	3.10	0.19	26.20	10.25	26.12	0.64	3.15	2189.03	5.09	5.27	204.81	16.80	29.70	44.08	–	5.44	5.68	17.99
Det. Lim.	0.05	0.05	0.02	0.05	0.05	0.05	0.16	0.03	0.45	0.15	0.01	0.07	0.04	0.01	0.23	0.19	0.003	0.01	0.31	0.004	0.03	0.01	0.004
MI29629 2/2 (n = 6)																							
Mean	0.29	0.65	0.07	56.42	2.02	0.67	0.26	293.75	353.61	3.09	3.93	4.81	0.67	3.16	7.80	137.22	0.25	118.58	2.62	0.010	3.70	14.48	242.58
Stand. Dev.	0.26	0.08	0.03	0.61	0.22	0.67	0.06	144.56	196.47	0.65	0.33	0.35	0.28	0.82	1.73	43.25	0.09	20.93	0.36	0.008	0.51	9.28	25.89
Maximum	0.58	0.75	0.10	57.48	2.36	0.78	0.33	426.57	579.26	4.17	4.27	5.33	1.17	4.55	11.28	185.06	0.36	158.42	2.97	0.022	4.35	31.22	284.15
Minimum	0.10	0.55	0.04	55.69	1.85	0.57	0.21	22.40	93.88	2.20	4.38	3.57	0.38	2.11	6.63	65.15	0.14	102.20	2.02	0.005	3.04	5.25	214.30
Median	0.10	0.66	0.07	56.41	1.91	0.67	0.25	318.53	337.72	2.99	3.93	4.85	0.62	3.14	7.22	140.15	0.24	112.53	2.65	0.006	3.57	13.60	238.13
Det. Lim.	0.05	0.05	0.02	0.05	0.05	0.05	0.19	0.02	0.45	0.16	0.01	0.07	0.04	0.01	0.23	0.21	0.003	0.01	0.28	0.005	0.03	0.01	0.003

–, not evaluated; <, under detection limit; LA-ICP-MS analyses: Internal standard = Fe; External standard, LODE_GSD-1G.
Stand. Dev. — standard deviation; Det. Lim. — detection limit.

TABLE 8. Major (EDS) and trace (LA-ICP-MS) element composition of hematite.

Sample	Al	Si	P	Fe	Zn	Pb	Ti	V	Cr	Mn	Co	Ni	Cu	Ga	Ge	As	Y	Mo	Cd	In	Sb	W	U
	wt.%						ppm																
BM1930-372 (n = 12)																							
Mean	–	1.38	–	62.03	0.53	3.21	0.89	96.01	8.33	11.78	0.46	3.40	71.37	14.20	10.21	156.99	4.89	175.15	6.48	0.10	25.57	111.86	18.65
Stand. Dev.	–	0.07	–	1.22	0.21	0.83	0.81	85.43	5.66	5.60	0.20	1.53	42.21	11.31	1.00	70.65	4.45	51.54	1.14	0.08	23.39	82.54	3.89
Maximum	<	1.50	<	63.68	0.90	4.45	1.82	264.19	22.13	23.33	1.07	8.13	140.70	43.88	11.62	253.47	11.04	254.90	8.29	0.20	64.73	237.88	25.41
Minimum	–	1.24	–	59.73	0.31	2.07	0.41	24.55	2.58	5.45	0.26	2.55	29.64	5.22	8.41	84.33	0.68	114.97	4.07	0.01	3.68	24.79	13.76
Median	–	1.38	–	62.19	0.48	2.79	0.44	58.93	6.47	11.11	0.39	2.90	61.52	10.42	9.94	131.73	2.86	153.21	6.75	0.10	18.23	91.67	16.75
Det. Lim.	0.05	0.05	0.02	0.05	0.05	0.05	0.41	0.04	0.96	0.23	0.01	0.10	0.09	0.02	0.43	0.30	0.005	0.02	0.27	0.01	0.07	0.02	0.004
MI29631 (n = 9)																							
Mean	0.32	1.46	–	62.15	0.71	–	68.17	94.10	46.98	350.63	59.44	24.17	145.75	6.90	4.28	180.79	2.73	57.32	6.32	35.85	211.84	31.35	25.05
Stand. Dev.	0.05	0.14	–	0.82	0.23	–	27.30	29.01	26.91	94.40	27.01	13.29	29.99	6.14	1.33	82.54	0.65	19.19	4.71	15.52	65.53	10.02	6.93
Maximum	0.36	1.67	<	63.30	1.13	<	93.38	152.00	83.03	421.47	107.57	47.99	201.43	19.89	5.77	326.76	3.19	86.49	16.35	60.15	346.82	42.09	33.47
Minimum	0.26	1.23	–	60.70	0.34	–	13.33	50.50	6.98	146.77	28.05	12.99	117.34	2.84	1.35	105.89	1.05	17.38	2.19	10.78	96.25	6.30	8.69
Median	0.33	1.43	–	61.88	0.67	–	79.01	85.71	59.47	402.30	62.30	16.06	133.48	3.06	4.69	144.97	2.85	60.86	3.75	38.37	210.96	34.15	25.24
Det. Lim.	0.05	0.05	0.02	0.05	0.05	0.05	0.34	0.03	0.77	0.21	0.01	0.10	0.07	0.02	0.34	0.25	0.004	0.01	0.25	0.01	0.05	0.01	0.004
OR5305 (n = 12)																							
Mean	–	1.24	–	60.40	0.88	4.66	0.49	229.88	19.90	576.47	43.06	14.74	59.88	1.24	3.57	458.56	1.11	478.00	10.75	0.01	10.08	88.03	277.80
Stand. Dev.	–	0.20	–	0.58	0.15	0.27	0.13	49.69	9.50	199.57	7.19	3.80	10.17	0.42	0.53	69.88	0.19	79.03	3.99	0.00	1.05	12.05	37.99
Maximum	<	1.67	<	60.99	1.10	5.15	0.77	372.35	38.10	906.99	62.04	25.65	73.65	2.26	4.41	530.02	1.43	642.48	22.91	0.02	11.53	98.98	338.81
Minimum	–	1.04	–	58.93	0.60	4.37	0.31	173.57	5.13	143.73	34.04	11.34	36.56	0.74	2.88	299.00	0.74	305.54	6.61	0.01	7.61	58.32	191.46
Median	–	1.17	–	60.55	0.90	4.57	0.47	218.23	22.15	536.89	43.05	13.98	60.42	1.13	3.53	483.63	1.15	489.01	9.90	0.01	10.20	92.87	278.63
Det. Lim.	0.05	0.05	0.02	0.05	0.05	0.05	0.25	0.03	0.65	0.22	0.01	0.10	0.05	0.01	0.33	0.25	0.004	0.01	0.23	0.01	0.05	0.02	0.005
MI29629 1/2 (n = 2)																							
Mean	–	0.53	–	63.66	1.36	2.29	28.67	1016.02	31.39	6.45	5.43	3.58	0.35	10.29	14.44	699.48	1.09	767.24	4.41	0.01	16.20	172.82	453.71
Stand. Dev.	–	0.20	–	0.60	0.37	0.30	8.70	795.29	28.74	2.99	4.22	1.75	0.25	13.67	7.35	110.75	0.33	549.96	0.66	0.00	2.56	46.93	247.71
Maximum	<	0.75	<	64.72	1.82	2.62	36.17	2429.12	81.41	9.89	12.70	5.86	0.72	34.57	23.51	824.35	1.57	1622.02	5.09	0.02	19.12	247.90	875.26
Minimum	–	0.25	–	63.28	0.95	2.04	18.09	570.52	10.13	3.59	2.55	1.74	0.20	1.82	5.25	566.95	0.69	295.96	3.42	0.01	13.43	138.62	256.83
Median	–	0.56	–	63.44	1.38	2.22	32.72	717.64	18.81	5.33	3.38	3.70	0.23	4.41	17.01	721.34	1.08	509.62	4.44	0.01	15.16	149.29	370.12
Det. Lim.	0.05	0.05	0.02	0.05	0.05	0.05	0.32	0.04	0.94	0.25	0.01	0.13	0.10	0.03	0.45	0.31	0.01	0.02	0.43	0.01	0.07	0.02	0.01
OR5309 (n = 22)																							
Mean	0.13	1.14	–	61.14	1.28	1.93	53.11	279.57	10.67	167.88	6.47	4.52	68.23	3.33	2.85	141.65	2.51	32.76	7.32	0.09	41.10	14.60	86.81
Stand. Dev.	0.05	0.09	–	1.20	0.43	0.34	20.77	90.75	13.11	42.09	2.85	1.22	17.65	0.66	0.42	39.60	0.53	13.32	3.12	0.05	8.41	2.55	45.33
Maximum	0.24	1.28	0.12	63.08	2.93	2.69	97.78	481.41	53.82	221.77	13.94	6.73	106.78	4.82	3.58	202.85	3.75	60.63	16.32	0.20	56.13	21.43	210.08
Minimum	0.00	0.98	0.12	59.02	0.88	1.42	29.05	110.93	0.78	83.62	3.49	2.87	48.20	2.20	1.91	78.50	1.65	16.45	3.55	0.03	26.93	10.53	43.30
Median	0.13	1.15	–	61.23	1.11	1.93	45.68	292.32	4.30	182.58	5.24	4.27	62.53	3.26	2.78	148.10	2.51	30.71	5.80	0.08	39.75	13.85	72.31
Det. Lim.	0.05	0.05	0.02	0.05	0.05	0.05	0.23	0.02	0.66	0.19	0.01	0.10	0.06	0.01	0.31	0.25	0.004	0.02	0.27	0.01	0.05	0.01	0.005
MI29629 2/2 (n = 4)																							
Mean	–	0.71	0.15	61.16	1.70	3.37	0.54	926.32	3999.69	14.19	14.06	1.88	0.51	1.54	7.19	1089.19	1.62	791.49	9.37	0.01	24.00	553.16	1103.63
Stand. Dev.	–	0.13	0.04	0.31	0.30	0.14	0.10	127.30	939.91	1.44	3.81	0.38	0.09	0.83	0.71	88.15	0.06	77.87	0.77	0.00	2.31	24.47	141.80
Maximum	<	0.79	0.19	61.63	2.07	3.54	0.66	1046.39	4722.16	16.15	18.98	2.36	0.58	2.76	8.21	1176.44	1.67	885.53	10.23	0.01	26.24	584.28	1264.46
Minimum	–	0.52	0.12	60.97	1.45	3.24	0.45	745.63	2684.78	12.71	10.30	1.47	0.38	0.93	6.58	970.69	1.56	695.34	8.50	0.00	21.90	533.03	926.40
Median	–	0.76	0.14	61.02	1.64	3.36	0.52	956.64	4295.90	13.95	13.48	1.85	0.53	1.24	6.99	1104.81	1.62	792.55	9.37	0.01	23.92	547.66	1111.83
Det. Lim.	0.05	0.05	0.02	0.05	0.05	0.05	0.28	0.03	0.66	0.23	0.01	0.14	0.06	0.02	0.36	0.37	0.01	0.01	0.51	0.01	0.04	0.01	0.004

–: element not detected; <: less than the detection limit; LA-ICP-MS analyses: Internal standard = Fe; External standard = LODE_GSD-1G.
Stand. Dev. — standard deviation; Det. Lim. — detection limit.

TABLE 9. Major (EDS) and trace (LA-ICP-MS) element composition of smithsonite.

Sample	Mg	Ca	Zn	Si	V	Mn	Fe	Cu	Ga	Ge	As	Cd	Pb
	wt.%			ppm									
BM1930-372 (n = 13)													
Mean	2.28	0.38	46.15	163.11	0.81	1041.84	621.95	9.15	0.95	–	4.61	2019.15	2060.54
Stand. Dev.	0.56	0.10	0.89	30.42	1.06	1852.57	430.90	13.74	0.42	–	3.23	1018.27	1126.51
Maximum	3.13	0.62	47.23	204.40	3.31	7180.84	1338.46	39.94	1.62	<	9.84	4041.24	4307.89
Minimum	1.38	0.22	44.50	110.58	0.04	189.28	123.97	0.17	0.28	–	0.77	497.93	343.27
Median	2.29	0.37	46.50	174.83	0.13	514.68	484.78	2.35	0.97	–	4.93	2050.45	2167.57
Det. Lim.	0.05	0.05	0.05	80.41	0.01	0.13	3.08	0.13	0.02	0.30	0.24	1.14	0.04

–: not evaluated; <: less than the detection limit; LA-ICP-MS analyses: Internal standard = Zn; External standard, LODE_NIST 610.
Stand. Dev. — standard deviation; Det. Lim. — detection limit.

TABLE 10. Major (EDS) and trace (LA-ICP-MS) element composition of descloizite.

Spectrum	V	Zn	Pb	Na	Mg	Al	Si	Ca	Cr	Mn	Fe	Co	Ni	Cu	Ga	Ge	As	Sr	Y	Zr	Mo	Cd
	wt.%					ppm																
OR5303 (n = 14)																						
Mean	12.41	15.67	52.20	8.83	150.99	85.06	240.84	725.83	509.36	6.07	15.76	4.20	23.32	2474.92	2.81	–	935.85	3.72	14.92	13.05	21.31	14.14
Stand. Dev.	0.19	0.53	0.67	9.17	29.11	35.53	127.95	251.19	196.20	4.66	11.61	1.43	5.71	992.43	1.02	–	369.57	1.29	6.96	10.54	5.57	3.53
Maximum	12.79	16.45	53.09	30.69	186.50	129.23	583.72	1053.31	963.74	14.20	39.77	7.89	37.07	4712.65	4.58	<	1907.39	6.38	24.43	29.50	30.41	24.80
Minimum	12.11	14.55	51.09	1.54	90.01	21.35	152.71	275.42	255.95	0.67	3.33	2.77	14.38	1527.69	0.91	–	425.76	1.75	2.03	0.33	12.67	9.72
Median	12.47	15.77	52.20	3.94	158.87	84.20	204.02	782.73	457.58	5.43	14.31	3.59	21.66	2229.42	2.80	–	874.93	3.77	17.31	11.57	22.17	13.62
Det. Lim.	0.02	0.05	0.05	1.07	0.05	0.29	49.25	19.21	0.29	0.09	1.90	0.01	0.04	0.10	0.01	0.09	0.17	0.002	0.002	0.003	0.01	0.37

–: not evaluated; <: less than the detection limit; LA-ICP-MS analyses: Internal standard = Zn; External standard = LODE_NIST 610.
Stand. Dev. — standard deviation; Det. Lim. — detection limit.
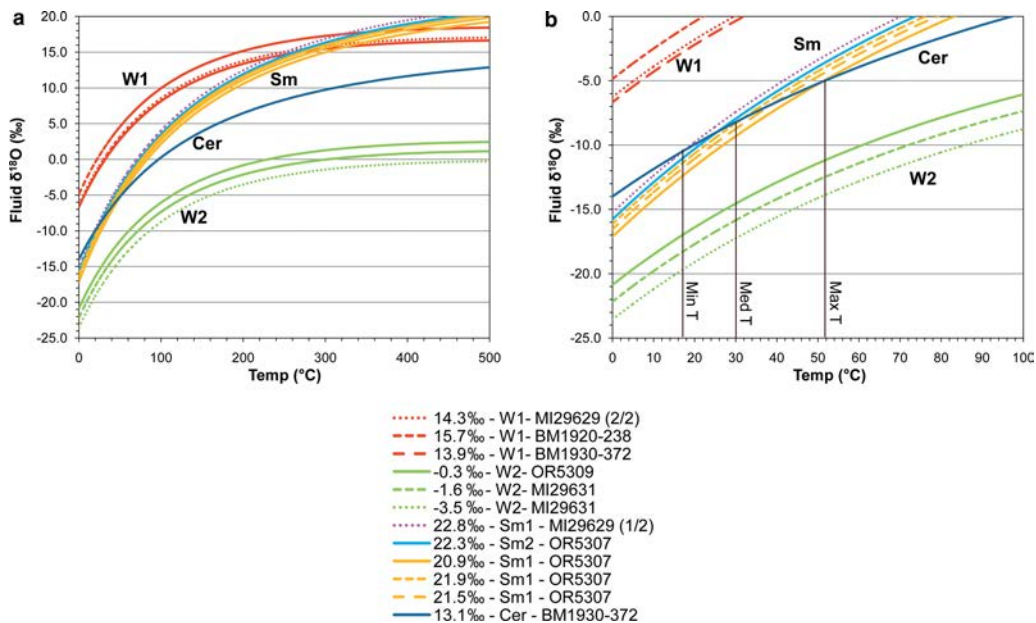
FIG. 7. (*a*) Mineral–fluid fractionation curves based on $\delta^{18}O$ ‰ V-SMOW of willemite 1 (red lines), willemite 2 (green lines), smithsonite 1 replacing sphalerite (magenta line), smithsonite 1 replacing dolomite (yellow lines), smithsonite 2 (light blue line), cerussite replacing galena (deep blue line). (*b*) Enlargement of (*a*).
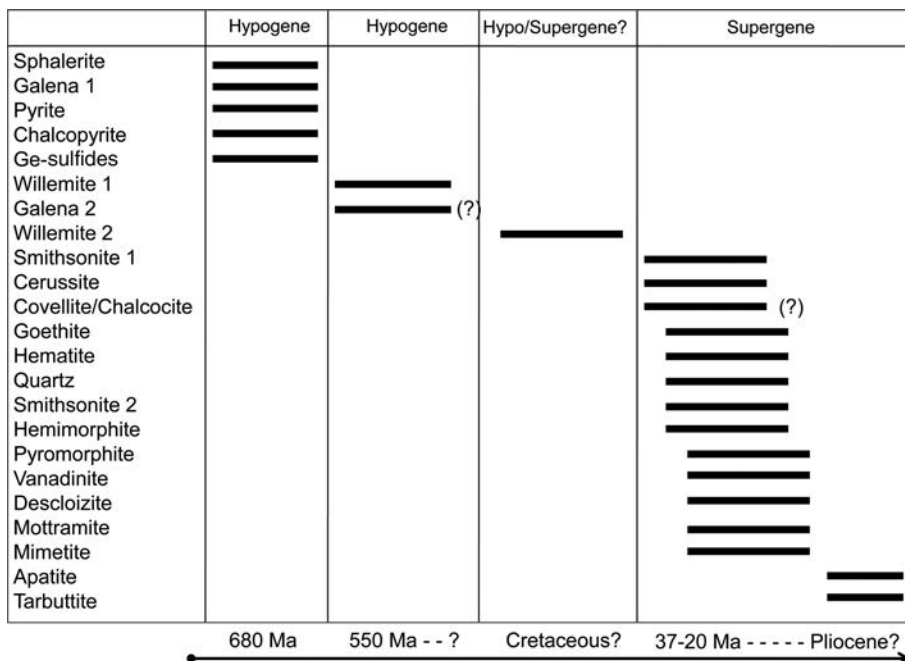

FIG. 8. Paragenesis of the hypogene and supergene minerals detected in the samples analysed from the Kabwe ores.

TABLE 11. Oxygen isotope composition of willemite.

Phase	Sample	$\delta^{18}O$ ‰$_{V\text{-SMOW}}$
Willemite 1	BM1920-238	15.7
	Duplicate-BM1920-238	15.6
	MI29629 2/2	14.3
	BM1930-372	13.9
	Duplicate-BM1930-372	14.0
	Mean	**14.7**
	Stand. Dev.	**0.9**
Willemite 2	MI29631 a	−1.6
	Duplicate-MI29631 a	−3.0
	Duplicate-MI29631 a	−4.6
	MI29631 b	−3.5
	Duplicate-MI29631 b	−3.0
	OR5309 b	−0.3
	Mean	**−2.7**
	Stand. Dev.	**1.5**

of precipitating fluids. In Fig. 7, it is possible to see that smithsonite (Sm1) and cerussite paths occupy a similar area, crossing at average ambient temperatures (~30°C) as expected, confirming that these two mineral species precipitated from weathering-related fluids. In contrast, W1 and W2 fractionation curves plot in two distinct areas of the diagram. W1 curves cross smithsonite curves at >300°C, an unreasonable estimate for smithsonite precipitation (Takahashi, 1960; Sangameshwar and Barnes, 1983; Gilg et al., 2008), confirming that W1 and smithsonite are not co-genetic. W2 paths cover an area of the graph very far from those of the other minerals, clearly out of a possible isotopic equilibrium with any other phase. Whilst not diagnostic, these isotopic data confirm that: (1) the two willemite generations are not co-genetic; and (2) neither W1 nor W2 is co-genetic with smithsonite or cerussite. Assuming this deduction, it follows that precipitation of willemites and

carbonates occurred: (1) from waters characterized by different isotopic composition; (2) from fluids having different temperatures; (3) at different times; or (4) one or more combinations of the previous three options.

Looking more in detail at the isotopic compositions of the supergene carbonate minerals, the smithsonite average composition (~21.9‰ V-SMOW) is seen to be less than that of supergene smithsonites from other mining areas of the world (~25–30‰ V-SMOW; Gilg et al., 2008; Boni and Mondillo, 2015). Cerussite (13.1‰ V-SMOW) also has smaller $\delta^{18}O$ values than other supergene cerussite (~15–20‰ V-SMOW; Gilg et al., 2008). Considering that smithsonite and cerussite were deposited at average ambient temperatures (~30°C), by using the cerussite-water and smithsonite-water oxygen isotope fractionation equations of Gilg et al. (2008), we calculated $\delta^{18}O$ compositions for the precipitating fluid of between ~−8 and ~−10‰. These $\delta^{18}O$ compositions for precipitating fluids, though slightly lower than the range of compositions already determined for mineralizing waters in other non-sulfide districts by Gilg et al. (2008), fall within the wider range of 'unusual' non-sulfide deposits already shown by Boni and Mondillo (2015, and references therein). In this case, the isotopic signatures of the Kabwe precipitating water must be related to the particular climatic conditions and to the location of the deposit at the time of the supergene alteration. Although a late Eocene–Oligocene age has been produced for the Kabwe descloizite (~20–37 Ma; N.J. Evans, unpubl., in Boni et al., 2007), by analogy with other supergene deposits occurring in this region (e.g. supergene Cu-Co and manganese deposits in the Katanga region; Dewaele et al., 2006; Decrée et al., 2010; Decrée et al., 2015; De Putter et al., 2015) and, more in general, in the southern African craton (Pack et al., 2000; Boni et al., 2007; Gutzmer et al., 2012; Arfè et al., 2017,

TABLE 12. C- and O-isotope compositions of smithsonite and cerussite.

Sample	Phase	Texture	$\delta^{13}C$ ‰$_{V\text{-PDB}}$	$\delta^{18}O$ ‰$_{V\text{-PDB}}$	$\delta^{18}O$ ‰$_{V\text{-SMOW}}$
MI29629 1/2	Smithsonite 1	smithsonite replacing sphalerite	−6.6	−7.9	22.8
BM1930-372	Cerussite	cerussite replacing galena	−11.1	−17.2	13.1
OR5307 a	Smithsonite 1	smithsonite replacing the host rock	−8.2	−9.7	20.9
OR5307 b	Smithsonite 1	smithsonite replacing the host rock	−5.0	−8.7	21.9
OR5307 c	Smithsonite 2	smithsonite crystal in cavity	−3.6	−8.4	22.3
OR5307 d	Smithsonite 1	smithsonite replacing the host rock	−6.2	9.1	21.5

and references therein), the ∼300–500 m deep (Kamona and Friedrich, 2007) supergene alteration profile at Kabwe could have formed during a period longer than the single descloizite age, possibly starting in the Late Cretaceous–early Eocene and extending until the Mio–Pliocene. In this time-frame, a tropical-humid climate persisted in the region and laterite profiles developed in the Katanga region (Giresse, 2005). At the same time, the region experienced various uplift stages, and reached the present height (∼1000 m a.s.l.) in the Miocene–Pliocene (De Putter *et al.*, 2015, and references therein). These conditions, together with the location of the Kabwe area in the inland of the southern African craton, could have produced groundwaters characterized by very negative $\delta^{18}O$ V-SMOW compositions (Mazor, 2004; Edmunds, 2005).

The nature of the fluids that precipitated the two willemite generations cannot be determined easily because the two silicates are not co-genetic and are not associated with any other oxidized mineral. Kamona and Friedrich (2007) consider the first willemite generation to be hydrothermal, and the second generation to be supergene, whereas Terracciano (2008) considers either a supergene or low-temperature hydrothermal origin for both of the willemite generations recognized here. Comparison of the $\delta^{18}O$ compositions of the Kabwe willemite with willemites from other deposits of the world is hampered by lack of data. At present, $\delta^{18}O$ compositions of willemite have been only measured at Sterling Hill (New Jersey, USA) (7.4–11.4‰ V-SMOW; Johnson *et al.* 1990), at Vazante (Minas Gerais, Brazil) (10.9–13.8‰ V-SMOW; Monteiro *et al.*, 1999), and at Bou Arhous (L'oriental Region, Morocco) (5.3–7.8‰ V-SMOW; Choulet *et al.*, 2017), where willemite is considered to be precipitated from hydrothermal fluids (Johnson *et al.* 1990; Monteiro *et al.*, 1999; Choulet *et al.*, 2017). Looking at the W1-water oxygen isotope fractionation curves, we see that for a limited range of temperatures only (∼0 to 40°C), the precipitating fluids would be characterized by the negative or slightly positive $\delta^{18}O$ compositions generally indicative of a relatively unaltered surface fluid origin in tropical latitudes. At temperatures greater than this, the measured W1 paths depict distinctly positive $\delta^{18}O$ compositions for the fluids. This, combined with the textural characteristics observed in field by Kamona (1993), and with the similarity between the $\delta^{18}O$ compositions of the Kabwe W1 and the previously reported hydrother-mal willemites, strongly suggests that W1 is also of

hydrothermal origin, given that the fluid O isotope compositions demand significant water–rock inter-action to obtain the positive values. W2 composi-tions map negative fluid $\delta^{18}O$ compositions at temperatures below ∼200°C, and only slightly positive values if they were precipitated at $T > 200°$C. $\delta^{18}O$ of the precipitating fluids could be very negative (from −20‰ to to −15‰ V-SMOW) at ambient temperatures, and slightly less negative (−10‰ V-SMOW) for temperatures of >60°C (hydrothermal fluids). Willemite with textures similar to W2 (i.e. euhedral hexagonal habit, with chemical oscillatory zoning) has been observed at Star Zinc (willemite II; Terracciano, 2008; Boni *et al.*, 2011), at Tres Marias (Saini-Eidukat *et al.*, 2009, 2016), and at Bou Arhous (Choulet *et al.*, 2017), where the mineral was considered to be of hydrothermal origin. If this was the case here, then clearly it was a distinctly different hydrothermal event compared to W1, given that the W2 precipitating fluid O isotope compositions, pre-serving a meteoric signature, are distinctly different from W1.

According to Kamona and Friedrich (2007), W1 may have formed shortly after the Lufilian Orogeny (∼550 Ma). Considering that the present data confirm that W1 at Kabwe is of hypogene origin, we agree with the latter authors on a possible post-'Lufilian' age for this phase. Boni *et al.* (2011) proposed the same age for another Zambian willemite mineralization, located at Star Zinc (willemite I; Terracciano, 2008; Boni *et al.*, 2011), near Lusaka. The age of W2 is more difficult to constrain, but considering the 'meteoric' signature of the precipitating fluids, it probably formed when the sulfide deposit was already exhumed, possibly in association with, or after, major Cretaceous uplifts (De Putter *et al.*, 2015 and references therein).

Critical-elements deportment

The critical elements Ga, In and Ge have a different deportment in the various minerals detected in the samples analysed. Gallium reaches tens of ppm only in sample BM1930-372, where the element has been detected directly in sphalerite, W1, goethite and hematite using LA-ICP-MS. Gallium concentrations in these minerals are not very high, but account for Ga levels measured in the bulk sample. Indium concentrations are above the detection limits only in sample MI29631, where it is found mostly in goethite and hematite, and in

trace amounts in willemite. In this case, there is a slight disagreement between the bulk-rock composition and In levels calculated using a combination of the PXRD mineral abundances and direct data from LA-ICP-MS of Fe-oxyhydroxides and willemite. This mismatch is probably due to errors in evaluating the average In concentration in willemite (which is the most abundant mineral in the sample). No In was detected in the sphalerite analysed. Germanium is above the detection limits in willemite- and Fe-oxyhydroxide-bearing samples, and in specimens containing sphalerite and willemite; moreover, it has been detected as discrete Ge-sulfides. Through LA-ICP-MS analysis, significant Ge ppm levels have been found in W1 and W2, and small traces of it in the supergene minerals (hemimorphite, goethite and hematite). The LA-ICP-MS data from these minerals together with mineralogical abundance account for the measured bulk-rock Ge contents, but note that Ge discrete minerals (e.g. sulfides or Ge-Fe-oxyhydroxides; see Melcher, 2003), may have been missed during our microanalytical study and could have created a slight mismatch between the measured bulk-rock Ge concentrations and mineral-phase analysis coupled with LA-ICP-MS data.

From these data, it is possible to infer that a remobilization of the elements occurred during the various stages of oxidation of the primary sulfides. Assuming that Ga, Ge and In originally occurred in sulfides, it appears that, when sulfides were initially altered to form the first willemite generation, W1 was only able to incorporate Ge and limited Ga. During the second oxidation stage, only Ge and limited In were incorporated into W2. Finally, during supergene oxide formation, Ga, In and Ge were comprehensively incorporated in different amounts into the Fe-oxyhydroxides. These different deportments among the various phases are probably controlled by three main factors: (1) differences in initial element abundance in the mineralization (Ge was probably more abundant than Ga and In in the primary sulfides); (2) variability in element solubilities at different temperatures and pH; and (3) the diverse affinity of the elements to the range of minerals formed.

At 25 and 100°C, the solubility of α-GaOOH has a minimum between pH = 2 and pH = 6 and increases at pH <2 and pH >6, solubility of GeO_2 is independent of pH at pH <8 and increases at pH <8, whereas the solubility of various In compounds has a broad minimum from pH ~4 to pH ~9 and increases for smaller and greater pH values (Wood and Samson, 2006). In addition, note that the most common oxidation states of Ga, In and Ge in aqueous solution are Ga^{3+}, In^{3+} and Ge^{4+}, and that at neutral pH, Ge is more soluble than both Ga and In (Wood and Samson, 2006). It follows that under certain conditions, the alteration of Ga-In-Ge-bearing sulfides can produce Ge-rich Ga-In-poor solutions, with Ga and In probably forming residual compounds in sulfides or oxyhydroxides. Germanium incorporation in willemite is not unusual, having already been observed in various Zn-silicate deposits, e.g. Franklin (Sheffer, 1966), Tsumeb (Lombaard et al., 1986), Beltana (Groves et al., 2003), Bou Arhous (Choulet et al., 2017) and Tres Marias (Saini-Eidukat et al., 2009, 2016). In particular, Saini-Eidukat et al. (2016) have described the structural occurrence of Ge in the Tres Marias willemite in detail, and have shown that "Ge in willemite occurs as Ge^{4+} and is four-fold coordinated with oxygen, as expected because the ionic radius of Ge^{4+} (0.44 Å) is close to that of Si^{4+} (0.39 Å) and isomorphism of Ge^{4+} with Si^{4+} is most probable". The fact that W1 and W2 contains more Ge than Ga and In could be related to the strong geochemical affinity between Ge and Si, but could also indicate that during the formation of W1 and W2, the Ge concentration in the precipitating fluids was greater than that of Ga and In. Willemite is stable at pH >7 in oxidizing environments (McPhail et al. 2003), and if solutions were particularly rich in Ge, Ge-bearing willemite could form in those conditions. Associated Fe-oxyhydroxides could also scavenge a range of elements having chemical affinities with Fe (Wood and Samson, 2006, and references therein). However, the present results suggest that Ge-bearing goethite is absent from the samples analysed, and both goethite and hematite have greater average Ga concentrations than either Ge or In. Considering the solubilities of the three elements, and assuming that the Fe-oxyhydroxides formed at ambient temperature and near-neutral pH (Wood and Samson, 2006), one explanation could be that during the last stage of supergene alteration of sulfides, Ge was leached progressively from the sulfides, whilst the more immobile Ga (under those pH and T conditions), was incorporated residually in newly formed Fe-oxyhydroxides, similar to the process which enriches Ga passively into bauxites (Wood and Samson, 2006). The same process could also explain the In concentration in the Fe-oxyhydroxides.

The present study revealed that at Kabwe, Fe-oxyhydroxides also host variable amounts of a range of other elements (Ca, Ti, V, Cr, Mn, Co, Ni, Cu, Ge, As, Y, Mo, Cd, In, Sb, W and U), which

could derive from weathering of the host rocks or the primary sulfide assemblage. Note that the elements Co, Ni, Cu, As, Mo, Cd, Sb and W, which have been not detected in the sphalerites or willemites analysed (and are unlikely to be present in the host rock at Kabwe or in other deposits of similar type, e.g. Tsumeb and Khusib Springs), are normally contained in Ge-bearing sulfides (Melcher, 2003).

Conclusions

Petrography has confirmed the complex paragenesis reported in previous studies on the Kabwe deposit. In the newly analysed samples, the relict sulfides consist mostly of sphalerite, containing Ge-sulfide inclusions, associated with 'interstitial' galena. The present authors suggest that this original sulfide association was altered by at least three oxidation stages: two stages that were dominated by the formation of willemite, and another characterized by deep weathering-related processes. The existence of these three stages is suggested by the oxygen isotope data, consistent with textural observations. $\delta^{18}O$ compositions of smithsonite (Sm1) and cerussite (replacing galena) suggest that both mineral species precipitated from weathering-related fluids. W1 and W2 have markedly different $\delta^{18}O$ compositions suggesting that the two willemite generations are not co-genetic. The $\delta^{18}O$ compositions and the textural characteristics of W1, resonating with those of previously reported hydrothermal willemites, strongly indicate a hydrothermal origin for W1. The distinct $\delta^{18}O$ composition of W2 indicates that this silicate precipitated from isotopically light fluids, probably of meteoric origin. There is no evidence to support either a supergene or a low-T hydrothermal origin for W2.

The critical elements Ga, In and Ge have a different deportment in the various minerals. Gallium has been detected at low ppm levels in sphalerite, W1, goethite and hematite, detectable but low values of In are found in goethite and hematite, whereas Ge forms proper sulfides, and occurs at low ppm levels in both W1 and W2, and in small traces in clearly supergene minerals (hemimorphite, goethite, hematite). The diverse deportments among the various phases are probably due to different initial Ga, In and Ge abundances in the sulfide mineralization, the different solubilities of the three elements at different temperatures and pH values, and finally to their different affinity for the neoformed mineral phases.

Supplementary material

To view supplementary material for this article, please visit https://doi.org/xxxxxx

References

Arfè, G., Boni, M., Balassone, G., Mondillo, N., Hinder, G. and Joachimski, M. (2017) New C-O isotopic data on supergene minerals from the Skorpion and Rosh Pinah ore deposits (Namibia): Genetic and paleo-climatic constraints. *Journal of African Earth Sciences*, **126**, 148–158.

Armstrong, R.A., Robb, L.J., Master, S., Kuger, F.J. and Mumba, P.A.C.C. (1999) New U–Pb age constraints on the Katangan sequence, Central African Copperbelt. *Journal of African Earth Sciences*, **28**, 6–7.

Arthurs, J.W., Newman, D. and Smith, A.G. (1995) Geology of the Chipembi area: explanation of degree sheet 1438, SE quarter. *Geological Survey of Zambia*, Report, **58**, 37 pp.

Barr, M.W.C., Cahen, L. and Ledent, D. (1978) Geochronology of syntectonic granites from Central Zambia: Lusaka granite and granite NE of Rufunsa. *Annales de la Société Géologique de Belgique*, **100**, 47–54.

Belissont, R., Boiron, M.-C., Luais, B. and Cathelineau, M. (2014) LA-ICP-MS analyses of minor and trace elements and bulk Ge isotopes in zoned Ge-rich sphalerites from the Noailhac–Saint-Salvy deposit (France): Insights into incorporation mechanisms and ore deposition processes. *Geochimica et Cosmochimica Acta*, **126**, 518–540.

Boni, M. and Mondillo, N. (2015) The "Calamines" and the "Others": The great family of supergene non-sulfide zinc ores. *Ore Geology Reviews*, **67**, 208–233.

Boni, M., Terracciano, R., Evans, N.J., Laukamp, C., Schneider, J. and Bechstädt, T. (2007) Genesis of vanadium ores in the Otavi Mountainland, Namibia. *Economic Geology*, **102**, 441–469.

Boni, M., Terracciano, R., Balassone, G., Gleeson, S.A. and Matthews, A. (2011) The carbonate-hosted willemite prospects of the Zambezi Metamorphic Belt (Zambia). *Mineralium Deposita*, **46**, 707–729.

Cahen, L., Snelling, N.J., Delhal, J. and Vail, J.R. (1984) *The Geochronology and Evolution of Africa*. Clarendon Press, Oxford, UK, 512 pp.

Cairney, T. and Kerr, C.D. (1998) The geology of the Kabwe area: explanation of degree sheet 1428, NW quarter. *Geological Survey of Zambia*, Report, **47**, 40 pp.

Choulet, F., Barbanson, L., Buatier, M., Richard, J., Vennemann, T., Ennaciri, A. and Zouhair, M. (2017) Characterization and origin of low-T willemite (Zn_2SiO_4) mineralization: the case of the Bou Arhous deposit (High Atlas, Morocco). *Mineralium Deposita*, **52**, 1085–1102.

Dare, S., Barnes, S.J., Beaudoin, G., Méric, J., Boutroy, E. and Potvin-Doucet, C. (2014) Trace elements in magnetite as petrogenetic indicators. *Mineralium Deposita*, **49**, 785–796.

Decrée, S., Deloule, E., Ruffet, G., Dewaele, S., Mees, F., Marignac, C., Yans, J. and De Putter, T. (2010) Geodynamic and climate controls in the formation of Mio-Pliocene world class oxidized cobalt and manganese ores in the Katanga province, DR Congo. *Mineralium Deposita*, **45**, 621–629.

Decrée, S., Pourret, O. and Baele, J.-M. (2015) Rare earth element fractionation in heterogenite (CoOOH): implication for cobalt oxidized ore in the Katanga Copperbelt (Democratic Republic of Congo). *Journal of Geochemical Exploration*, **159**, 290–301.

De Putter, T., Ruffet, G., Yans, J. and Mees, F. (2015) The age of supergene manganese deposits in Katanga and its implications for the Neogene evolution of the African Great Lakes Region. *Ore Geology Reviews*, **71**, 350–362.

Dewaele, S., Muchez, P., Vets, J., Fernandez-Alonzo, M. and Tack, L. (2006) Multiphase origin of the Cu–Co ore deposits in the western part of the Lufilian fold-and-thrust belt, Katanga (Democratic Republic of Congo). *Journal of African Earth Sciences*, **46**, 455–469.

Edmunds, W.M. (2005) Groundwater as an archive of climatic and environmental change. Pp. 341–352 in: *Isotopes in the Water Cycle: Past, Present and Future of a Developing Science* (P.K. Aggarwal, J.R. Gat and K.F.O. Froehlich, editors). Springer, Berlin.

Gilg, H.A., Boni, M., Hochleitner, R. and Struck, U. (2008) Stable isotope geochemistry of carbonate minerals in supergene oxidation zones of Zn–Pb deposits. *Ore Geology Reviews*, **33**, 117–133.

Giresse, P. (2005) Mesozoic-Cenozoic history of the Congo Basin. *Journal of African Earth Sciences*, **43**, 301–315.

Groves, I., Carman, C.E. and Dunlap, W.J. (2003) Geology of the Beltana willemite deposit, Flinders Ranges, South Australia. *Economic Geology*, **98**, 797–818.

Gutzmer, J., Du Plooy, A.P. and Beukes, N.J. (2012) Timing of supergene enrichment of low-grade sedimentary manganese ores in the Kalahari Manganese Field, South Africa. *Ore Geology Reviews*, **47**, 136–153.

Heijlen, W., Banks, D.A., Muchez, P., Stensgard, B.M. and Yardley, B.W.D. (2008) The nature of mineralizing fluids of the Kipushi Zn-Cu deposit, Katanga, Democratic Republic of Congo: quantitative fluid inclusion analysis using Laser Ablation ICP-MS and bulk Crush-Leach methods. *Economic Geology*, **103**, 1459–1482.

Hitzman, M.H., Reynolds, N.A., Sangster, D.F., Allen, C.R. and Carman, C.E. (2003) Classification, genesis, and exploration guides for nonsulphide zinc deposits. *Economic Geology*, **98**, 685–714.

Intiomale, M.M. (1982) *Le Gisement Zn–Pb–Cu de Kipushi (Shaba, Zaïre). Etude Géologique et Métallogénique*. PhD dissertation, Université Catholique de Louvain, Belgium.

Johnson, C.A., Rye, D.M. and Skinner, B.J. (1990) Petrology and stable isotope geochemistry of the metamorphosed zinc-iron-manganese deposit at Sterling Hill. New Jersey. *Economic Geology*, **85**, 1133–1161.

Kamona, A.F. (1993) *The Carbonate-Hosted Kabwe Pb–Zn Deposit, Central Zambia*. PhD dissertation, Technical University of Aachen, Aachen, Germany.

Kamona, A.F. and Friedrich, G.H. (2007) Geology, mineralogy and stable isotope geochemistry of the Kabwe carbonate-hosted Pb–Zn deposit, Central Zambia. *Ore Geology Reviews*, **30**, 217–243.

Kamona, A.F., Lévêque, J., Friedrich, G. and Haack, U. (1999) Lead isotopes of the carbonate-hosted Kabwe, Tsumeb, and Kipushi Pb–Zn–Cu sulphide deposits in relation to Pan African orogenesis in the Damaran–Lufilian fold belt of Central Africa. *Mineralium Deposita*, **34**, 273–283.

Kampunzu, A.B., Cailteux, J.L.H., Kamona, A.F., Intiomale, M.M. and Melcher, F. (2009) Sediment-hosted Zn-Pb-Cu deposits in the Central African Copperbelt. *Ore Geology Reviews*, **35**, 263–297.

Kortman, C.R. (1972) The geology of the Zambia Broken Hill Mine, Kabwe. *Geologie en Mijnbouw*, **51**, 347–356.

Large, D. (2001) The geology of nonsulphide zinc deposits – an overview. *Erzmetall*, **54**, 264–276.

Leach, D.L., Sangster, D.F., Kelley, K.D., Large, R.R., Garven, G., Allen, C.R., Gutzmer, J. and Walters, S. (2005) Sediment-hosted lead-zinc deposits: A global perspective. *Economic Geology*, *100th Anniversary Volume*, 561–607.

Lombaard, A.F., Günzel, A., Innes, J. and Krüger, T.L. (1986) The Tsumeb lead–copper–zinc–silver deposit, South West Africa/Namibia. Pp. 1761–1782 in: *Mineral Deposits of Southern Africa*, Vol. 2 (C.R. Anhaeusser and S. Maske, editors). Geological Society of South Africa, Johannesburg.

Longerich, H.P., Jackson, S.E. and Günther, D. (1996) Laser ablation inductively coupled plasma mass spectrometric transient signal data acquisition and analyte concentration calculation. *Journal of Analytical Atomic Spectrometry*, **11**, 899–904.

Master, S., Rainaud, C., Armstrong, R.A., Phillips, D. and Robb, L.J. (2005) Provenance ages of the Neoproterozoic Katanga Supergroup (Central African Copperbelt), with implications for basin evolution. *Journal of African Earth Sciences*, **42**, 41–60.

Mazor, E. (2004) *Chemical and Isotopic groundwater hydrology*. Marcel Dekker, Inc., New York, 453 pp.

McPhail, D.C., Summerhayes, E., Welch, S. and Brugger, J. (2003) The geochemistry of zinc in the regolith. Pp. 287–291 in: *Advances in Regolith* (I.C. Roach, editor). Landscape Environments and Mineral Exploration, CRC Press, Florida, USA.

Melcher, F. (2003) The Otavi Mountain Land in Namibia: Tsumeb, germanium and snowball earth. *Mitteilungen der Österreichischen Mineralogischen Gesellschaft*, **148**, 413–435.

Monteiro, L.V.S., Bettencourt, J.S., Spiro, B., Graca, R. and Oliveira, T.F. (1999) The Vazante zinc mine. Minas Gerais, Brazil: constraints on willemitic mineralization and fluid evolution. *Exploration Mining Geology*, **8**, 21–42.

Moore, T.A. (1964) The geology of the Chisamba area: explanation of degree sheet 1428, SW quarter. *Geological Survey of Zambia*, Report, **5**, 32 pp.

Pack, A., Gutzmer, J., Beukes, N.J., van Niekerk, H.S. and Hoernes, S. (2000) Supergene ferromanganese wad deposits derived from Permian Karoo strata along the Late Cretaceous–Mid-Tertiary African land surface, Ryedale, South Africa. *Economic Geology*, **95**, 203–220.

Porada, H. and Berhorst, V. (2000) Towards a new understanding of the Neoproterozoic–Early Palaeozoic Lufilian and northern Zambezi belts in Zambia and the Democratic Republic of Congo. *Journal of African Earth Sciences*, **30**, 727–771.

Saini-Eidukat B., Melcher F. and Lodziak J. (2009) Zinc-germanium ores of the Tres Marias Mine, Chihuahua, Mexico. *Mineralium Deposita*, **44**, 363–370.

Saini-Eidukat, B., Melcher, F., Göttlicher, J. and Steininger, R. (2016) Chemical environment of unusually Ge- and Pb-rich willemite, Tres Marias Mine, Mexico. *Minerals*, **6**, 20.

Samama, J.C., Mapani, B. and Tembo, D. (1991) Breccias and their use in paleoenvironmental studies: Kabwe zinc deposit (Zambia). *Zambian Journal of Applied Earth Sciences*, **4**, 22–29.

Sangameshwar, S.R. and Barnes, H.L. (1983) Supergene processes in zinc-lead-silver sulfide ores in carbonates. *Economic Geology*, **78**, 1379–1397.

Sharp, Z.D. (1990) A laser-based microanalytical method for the in situ determination of oxygen isotope ratios in silicates and oxides. *Geochimica et Cosmochimica Acta*, **54**, 1353–1357.

Sheffer, H.W. (1966) The occurrence of germanium in willemite. *Geochimica et Cosmochimica Acta*, **30**, 837–838.

Takahashi, T. (1960) Supergene alteration of zinc and lead deposits in limestone. *Economic Geology*, **55**, 1083–1115.

Taylor, J.H. (1954) The lead–zinc–vanadium deposits at Broken Hill, northern Rhodesia. *Colonial Geology and Mineral Resources*, **4**, 335–365.

Taylor, J.H. (1958) The formation of supergene galena at Broken Hill, northern Rhodesia. *Mineralogical Magazine*, **31**, 908–913.

Terracciano, R. (2008) *Willemite Mineralisation in Namibia and Zambia*. PhD dissertation, Università degli Studi di Napoli Federico II, Italy, 178 pp.

Whyte, W.J. (1966) Geology of the Broken Hill Mine, Zambia. Pp. 395–425 in: *Symposium on Lead–Zinc Deposits in Africa*. Association of African Geological Surveys, Tunis Meeting, April 1966, **Vol. 23**.

Wood, S.A. and Samson, I.M. (2006) The aqueous geochemistry of gallium, germanium, indium and scandium. *Ore Geology Reviews*, **28**, 57–102.

Zachariáš, J. and Wilkinson, J. (2007) *ExLAM 2000: excel VBA application for processing of transient signals from laser ablation (LA-ICPMS) of fluid inclusions and solid phases*. ECROFI-XIX Biennial conference on European current research on fluid inclusions, Bern, Switzerland.

Zheng, Y.F. (1993) Calculation of oxygen isotope fractionation in anhydrous silicate minerals. *Geochimica et Cosmochimica Acta*, **57**, 1079–1091.